Department of Electrical and Computer Engineering

Technical University of Munich

Master's Thesis

Reducing the Cross-Polarization Level of a Compact Antenna Test Range by a Realization of the Conjugate Matched Field Concept

Michael Pircher

Department of Electrical and Computer Engineering

Technical University of Munich

Master's Thesis

Reducing the Cross-Polarization Level of a Compact Antenna Test Range by a Realization of the Conjugate Matched Field Concept

Author:	Michael Pircher
Supervisor:	Univ.-Prof. Dr.-Ing. Thomas Eibert
Advisors:	Dipl.-Ing. Markus Limbach
	Dr.-Ing. Tobias Rommel
Submission Date:	14.09.2022

I confirm that this master's thesis is my own work and I have documented all sources and material used.

Munich, 14.09.2022 Michael Pircher

Acknowledgments

First, I would like to express my gratitude to Univ.-Prof. Dr.-Ing. Thomas Eibert from the Technical University Munich, for making it possible to write this thesis at an external research institute and for his excellent supervision.

This research would not have been possible without my supervisors from the antenna group at the Microwaves and Radar Institute: Dipl.-Ing. Markus Limbach and Dr.-Ing. Tobias Rommel. I am very grateful for their professional advises and for showing me the way toward a scientific career. Special thanks also to Dipl.-Ing. Bernd Gabler for the countless hours of field probe measurements in the compact test range. Many thanks to Christoph Wessel from the mechanical laboratory, for supporting the construction process of the antenna and its manufacturing. I would like to thank all other members of the antenna group for the inspiring talks and their helpful inputs. Thanks should also go to Prof. Dr. Andreas Reigber, the head of the SAR technology department, and to Prof. Dr.-Ing. Alberto Moreira, the director of the Microwaves and Radar Institute.

Abstract

In antenna measurements it is well known that single reflector and dual cylindrical reflector Compact Antenna Test Ranges (CATRs) suffer from a high cross-polarization level in the Quiet Zone (QZ). This limits their performance of measuring an Antenna under Test (AUT) with high cross-polar suppression. This issue is avoided by the development of a new three element feed array. The central horn antenna ensures the co-polar field, while the outer horns generate the so called conjugate matched field and hence reduce the cross-polarization. A nonlinear, numerical optimization is used to calculate the weighting factors of each element. It must consider also the limitations of the prototype-based feeding network. The feed array is capable of generating horizontally and vertically polarized waves and it operates in the X-band.

The performance of the feed array is validated in High-Frequency Structure Simulator (HFSS) simulations, where an improvement of 8 dB in the cross-polar level is found in the QZ. A proof of concept demonstrator is measured in the Compact Test Range (CTR) of the Microwaves and Radar Institute of the German Aeorspace Center (DLR). A field probe scan shows a mean cross-polar level of -41.6 dB, over 9 dB better than the currently used reference. The cross-polarization is effectively reduced over a bandwidth of 900 MHz.

Zusammenfassung

Die hohe Kreuzpolarisation in der Messzone von Einzelreflektor Messanlagen, beziehungsweise von dual-zylindrischen Compact Antenna Test Ranges (CATRs) ist ein bekanntes Problem in der Antennenmesstechnik. Es limitiert die Möglichkeit des Messsystems Antennen zu charakterisieren, die eine hohe Kreuzpolarisationsunterdrückung aufweisen. Das Problem wird durch eine neue Speise-Gruppenantenne gelöst, welche aus drei Elementen besteht. Das zentrale Horn generiert das kopolare Feld, während die beiden äußeren Hörner das so genannte konjugiert angepasste Feld erzeugen und dadurch die Kreuzpolarisation in der Messzone reduzieren. Eine nichtlineare numerische Optimierung berechnet die Gewichtungsfaktoren für jedes Antennenelement. Der Optimierungsalgorithmus berücksichtigt auch die begrenzten Möglichkeiten des Speisenetzwerks im Stadium eines Prototypen. Die Speise-Gruppenantenne kann sowohl horizontal als auch vertikal polarisierte elektromagnetische Wellen erzeugen und arbeitet im X-Band.

Die Leistungsfähigkeit der Gruppenantenne wird im High-Frequency Structure Simulator (HFSS) validiert. In der Simulation ist eine Verbesserung der mittleren Kreuzpolarisation der Messzone von 8 dB bemerkbar. Der Demonstrator wird in der Compact Test Range (CTR) des Instituts für Hochfrequenztechnik und Radarsysteme am DLR vermessen. Ein Scan mit einer Feldsonde bestätigt ein mittleres kreuzpolares Level von -41.6 dB, eine Verbesserung von über 9 dB verglichen mit der Referenzantenne. Die effektive Kompensation der Kreuzpolarisation findet in einer Bandbreite von 900 MHz statt.

Acronyms

SAR	Synthetic Aperture Radar
CTR	Compact Test Range
CATR	Compact Antenna Test Range
DLR	German Aeorspace Center
AUT	Antenna under Test
NF/FF	Near Field to Far Field
QZ	Quiet Zone
GO	Geometrical Optics
HFSS	High-Frequency Structure Simulator
SBR	Shooting and Bouncing Rays
PEC	Perfect Electric Conductor
UTD	Uniform Theory of Diffraction
PTD	Physical Theory of Diffraction
PO	Physical Optics
IEEE	Institute of Electrical and Electronics Engineers
KKT	Karush-Kuhn-Tucker
RCS	Radar Cross Section

Contents

1 Introduction

Modern earth observation gathers important data for a large variety of application: cartography, climatology, reconnaissance, civil protection and many more. Under the different methods of earth observation Synthetic Aperture Radar (SAR) plays a key role and has several advantages, with respect to other sensors like optical or infrared. It can operate nearly independent of weather and day time. Additionally, SAR systems can be used on a variety of platforms. With the TanDem-X satellites the Microwaves and Radar Institute of the German Aeorspace Center (DLR) also operates a SAR mission in space [1, pp. 468][2].

In the 1980s considerable improvement was achieved by developing the first polarimetric SAR systems. The polarization of the illuminating wave has a direct influence on the scattering properties of the observed scene. This can be used to gather additional information from the images. Polarimetric SAR systems are designed to transmit and receive waves with orthogonal polarization states, mostly vertically and horizontally. Given this configuration four polarization states of the same scene are measured: Horizontally transmitted and horizontally received, or short HH. Additionally, there exist: VV, HV and VH. Due to reciprocity the HV- and VH-states are the same, so that in total three states are measured [1, p. 455]. In different fields of applications these polarization states are used for a more detailed analysis. For example it allows an estimation of the biomass in forests. Also for urban applications such data are important, since man made objects have a characteristic polarimetric backscattering [3, pp. 59, 215]. A crucial part of such systems are the antennas. In order to resolve the different polarization states dual polarized antennas with a very low cross-polarization are needed. The Microwave and Radar Institute of the DLR does a lot of research in such antennas, which are measured inhouse in a dual parabolic cylindrical Compact Test Range (CTR).

The CTR consists of two reflectors which are illuminated by a feed antenna. Both reflectors ensure that the unknown Antenna under Test (AUT) is illuminated adequately, by a locally plane wave. While this principle is well suited for regular measurements, it reaches its limits by measuring low cross-polar values. In this case the AUT must be illuminated by a wave free of cross-polarization, otherwise the results get corrupted. During the measurement it is not possible to distinguish between cross-polarization generated by the AUT or by the illuminating wave. The CTR at the DLR suffers, like all others of this type, from a non ideal polarization, caused by the offset geometry.

The depolarization property of an offset fed reflector antenna was first discussed in [4]. It is a solely analytical analysis, showing a strong relation between the cross-

polarization level and the offset angle. In the center of the aperture, along the symmetry line of the reflector, the cross-polarization is zero, but towards the upper and lower end of the aperture it increases. In [5] the same effect is described for dual parabolic cylindrical Compact Antenna Test Ranges (CATRs). Besides the offset angle, an increase in the focal length of the reflectors decreases the cross-polarization.

A so called compensated CTR does not suffer from a high cross-polar level. Its sub-reflector is shaped to illuminate the main-reflector properly without generating cross-polarization [6]. Another solution is to apply the conjugate matched field concept. The cross-polar radiation pattern of the feed is modified, that it destructive interferes with the offset-caused cross-polarization. In the aperture, where the AUT is placed, a purely polarized wave occurs. Different methods exist to ensure the conjugate matched field. In [7] polarization grids are placed in front of the feed antenna. Others, like [8] use tri-mode feeds and have proven it successfully, but for a limited bandwidth of 250 MHz in the X-band (8 GHz to 12 GHz). The most compromising results are found in [9], where a three element feed array is used. A more detailed comparison of the compensation techniques is conducted in the thesis.

The main goal of this thesis is to use the conjugate matched field concept to reduce the cross-polarization in the DLR's CTR. Like in [9] a three element array is used and a nonlinear numerical optimization determines the complex weighting factors. The development process includes not only a simulative approach in High-Frequency Structure Simulator (HFSS), also a proof of concept demonstrator is build. The feed antenna must operate in the X-band, since it is often used for radar applications, but the concept should be scalable to other frequencies. In order to develop the feed, the cross-polarization of the CTR in current configuration, must be analyzed. This is done by simulations as well as by direct measurements with a field scanner.

The thesis starts with the fundamentals in chapter 2. This includes a discussion about the property of polarization and antenna measurement in general. Different antenna ranges are presented, with a special focus on the CTR at the Microwaves and Radar Institute of the DLR. Chapter 2 concludes with an overview of numerical optimization techniques, which will be used to increase the performance of the new feed.

In chapter 3 the cross-polarization generated by the CTR is analyzed. First it is done by simulations in HFSS and than by measurements with a field scanner. The second part of this chapter presents the development process, leading to a new feed array, which is capable of reducing the cross-polarization. A proof of concept demonstrator is manufactured in the institute's mechanical lab.

The chapter 4 compares the resulting co- and cross-polar performance of the new developed feed array with the currently used feed horn. The comparison is done by simulation results as well as by field probe measurements.

In the closing chapter 5 a conclusion is made, including the advantages and disadvantages of the new feed design. An outlook on future task is given, including a solution for increasing the bandwidth over the entire X-band.

The exact positions of the reflectors, representing the geometry of the CTR are sensitive data. Therefore they are truncated after the first decimal place.

2 Fundamentals

This chapter summarizes the function principle of different antenna measurement techniques, including its technical and physical limitations. The consequences of the limitations on the results are presented, especially considering the cross-polarization level. First, the property of polarization is explained in general and in which way different antenna positioning systems affect the polarization bases. The chapter concludes with a discussion of measurement range principles, and an extensive examination of CATRs.

2.1 Polarization

Polarization is an inherent property of electromagnetic waves and, in addition to frequency, phase, amplitude, and the observation point one of five key characteristics of a sinusoidal electromagnetic wave. In [10, p. 66] the polarization of a radiated wave is defined as "that property of an electromagnetic wave describing the time varying direction and relative magnitude of the electric field vector; specifically, the figure traced as a function of time by the extremity of the vector at a fixed location in space, and the sense in which it is traced, as observed along the direction of propagation". In the Institute of Electrical and Electronics Engineers (IEEE) Standard for Definitions of Terms of Radio Wave Propagation [11] the polarization of an electromagnetic wave is defined by "The locus of the tip of the electric field vector observed over time at a fixed point in space in a plane orthogonal to the wave normal".

Both definitions mean the same: The changing electric field vector is observed at a fixed observation point over time. The trace, the vector over time describes, allows to classify the polarization. In order to visualize the definition, two plane waves are shown in Fig. 2.1 and in Fig. 2.2. The electric field vector in Fig. 2.1 moves along a straight line in x-direction, and represents a linearly polarized wave. In Fig. 2.2 the instantaneous field vector describes a circular trace with ongoing time. Looking in the direction of propagation the vector rotates clockwise over time, giving a right hand polarization [12, pp. 82][13, pp. 61].

Additionally, the term polarization is used in context of antennas. It is defined by the polarization of the wave, radiated by the antenna. It depends on the angular direction. In case no particular direction is defined, it is assumed to be in main beam. Since antennas can only radiate fully polarized fields, exclusively these types are discussed in the following sections [13, p. 65][14, p. 11].

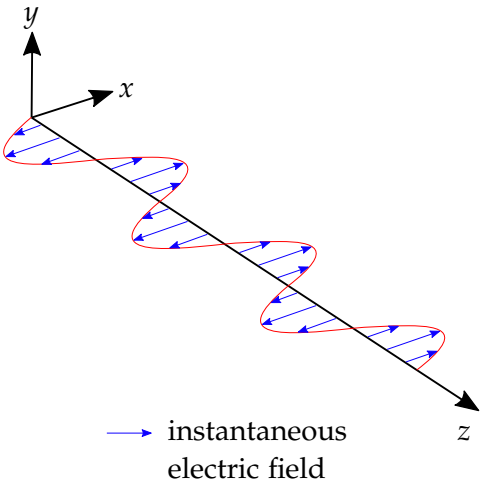

Fig. 2.1: Linear polarized plane wave propagating in z-direction, adapted from [12, p. 82].

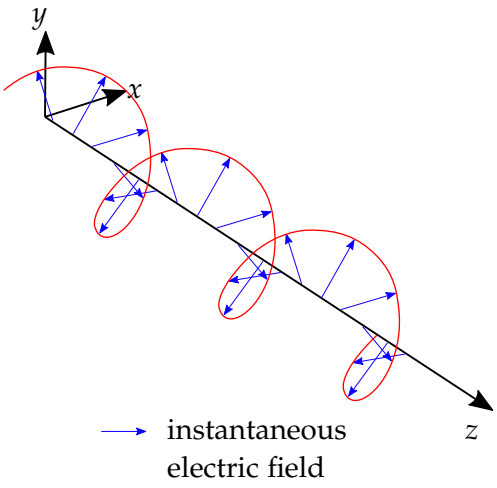

Fig. 2.2: Right hand circular polarized wave, with direction of propagation in z [12, p. 82].

2.1.1 Polarization Ellipse

The linear and circular polarization states, shown in Fig. 2.1 and Fig. 2.2 are special cases. In general, a fully polarized wave has elliptical polarization, which is derived in [14, pp. 27]. In the following discussion the concept of the polarization ellipse is introduced, as a useful tool for visualization.

Any polarization can be decomposed in two orthogonal states. For example, a time harmonic plane wave propagating in z-direction

$$\vec{E}(t,z) = E_x(t,z)\vec{e_x} + E_y(t,z)\vec{e_y}\,, \tag{2.1}$$

can be constructed by a x-component

$$E_x(t,z) = E_1\cos(\omega t - \beta z)\,,$$

and a y-component

$$E_y(t,z) = E_2\cos(\omega t - \beta z + \delta)\,,$$

where ω stands for the angular frequency, E_1 and E_2 are the maximum amplitudes of the electric field of the x- and y-component respectively. The phase constant is denoted by β, $\vec{e_x}$ and $\vec{e_y}$ represent the unit vectors in x- and y-direction. Both waves are shifted with respect to each other by a phase difference δ. In [14, pp. 27] it is proven that the electric field vector of the plane wave, expressed in (2.1), describes an elliptical trace over time. It is mathematically evident to describe the polarization by an ellipse, as shown in Fig. 2.3. The length of the major and minor axis is denoted by a, and b. In a physical context these parameters are associated to the maximum and minimum

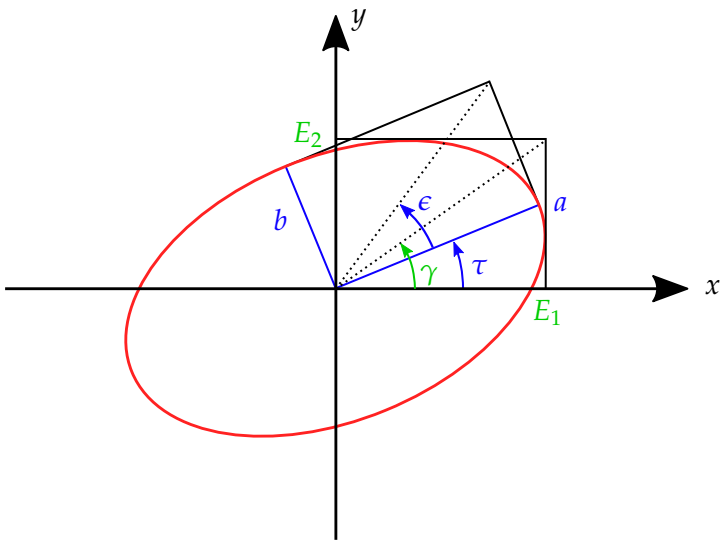

Fig. 2.3: The polarization ellipse, drawn in red color, including all relevant quantities to describe the polarization state, adapted from [14, p. 31].

electric field. They are mandatory to calculate the ellipticity angle

$$\chi = \cot^{-1}\left(-\frac{a}{b}\right) .$$

The tilt angle τ is between x-axis and the major axis of the ellipse. Both quantities, χ and τ, allowing unique definition of the polarization ellipse and therefore, the polarization state.

A second possibility to uniquely describe the polarization state is given by introducing

$$\gamma = \tan^{-1}\left(\frac{E_2}{E_1}\right) ,$$

together with the phase difference, δ. This means, based on the polarization ellipse, two different types of definition methods exist [14, pp. 31]. For example, a right hand circular polarized wave (like shown in Fig. 2.2) is fully described by an ellipticity angle of $\chi = -45°$ and the tilt angle τ is irrelevant. The same wave is also completely defined by $\gamma = 45°$ and a phase difference of $\delta = -90°$.

An important addition is to state, that the decomposition of (2.1) is not restricted to Cartesian coordinates. The electric field vector can be resolved on any other orthogonal system. Especially in antenna measurement, it is convenient to use a spherical coordinate system. Important different decompositions of the field vector will be discussed in Section 2.2.2 [14, p. 33].

2.1.2 Co- and Cross-polarization

In the IEEE Standard for Definitions of Terms of Antennas [15] cross-polarization is defined as "the polarization orthogonal to a specified reference polarization". But no statement is made, what the reference polarization is. This allows to define the direction of the reference dependent on the application. One example is a polarization sensitive transmission. Many antennas have a preferred polarization, any incoming signal with a polarization perpendicular to the reference (co-polar signal) is received ideal. A cross-polar wave (having a polarization state orthogonal with respect to the reference) is not detectable [12, p. 215][16, pp. 698].

The topic of co- and cross-polarization is directly affected by the coordinate system chosen to represent the electromagnetic wave. In practice three systems are used: Cartesian, spherical and the so called Ludwig III coordinate system. All systems are presented in greater detail in Section 2.2.2 [17].

2.2 Antenna Measurements

Antenna systems are characterized by different parameters. In the further course of this thesis only the high frequency properties of antennas are of interest. According to [10, pp. 25], the most important quantities are:

- Radiation pattern, $C(\theta, \phi)$: It describes the angular variation of the radiated electric field in far field.
- Gain, G: The gain is defined in a given direction. It is the ratio between the radiation intensity in the considered direction, and the intensity of an isotropic radiator. In rare cases the radiation intensity of the antenna is referenced to a $\lambda/2$ dipole.
- Antenna radiation efficiency, η: It is defined as the ratio of the power radiated by an antenna to the total power accepted by the antenna [15]. The antenna radiation efficiency considers both dielectric and conduction losses.
- Directivity, D: The directivity is related to the gain by η according to the formula $D = G/\eta$.
- The polarization of an antenna is defined by the polarization the transmitted wave has. It can vary depending on the angular direction. In Section 2.1 a more comprehensive discussion of a polarized wave is given [15].
- Input impedance, Z_{in}: The input impedance allows the calculation of the reflection coefficient, and is defined as the ratio between voltage and current at the antenna's feed point.

For antenna radiation pattern measurements at least two antennas are needed. One operates in receiving mode, and the other one is transmitting. The unknown antenna is usually receiving, and it is called AUT. The transmitting structure is denominated range antenna or feed. The determination of all far field quantities requires an illumination of the AUT by a plane wave. Its property is that the phase fronts (the points of constant phase) are aligned in a plane, which is orthogonal to the direction of propagation. A perfect plane wave is physically not realizable, but it can be approximated by a locally plane wave. This means that in a finite extension the amplitude and phase error of the wave are below a specified value. The aim of the feed is to generate a desired plane wave, which illuminates the AUT [12, p. 62]. In Near Field to Far Field (NF/FF) techniques the electric field is measured in the near field. They do not require a locally plane wave and are not topic of this discussion. Further information can be found in [10, pp. 992][16, pp. 355].

The methods, which are used to generate a locally plane wave are discussed later. In the following the general measuring procedure is presented, assuming the AUT is illuminated properly.

2.2.1 Measurement without Polarization Characteristic

Both, polarization and radiation intensity of an antenna are angular dependent therefore, the measurement of these properties is more challenging. For simplicity, in this section it is assumed that the AUT is illuminated by a plane wave and not polarization sensitive. The AUT is placed on a rotary positioning system (called positioner), which allows to point the antenna in any direction. The orientation of the AUT has three degrees of freedom, it can be rotated around the x-axis, y-axis and the z-axis. The arrangement is visualized in Fig. 2.4. It can be seen in Fig. 2.4 that a rotation of the AUT around two angles is sufficient to cover all directions. One rotation can be fixed. This corresponds to three possible combinations and each of them describes one type of spherical coordinate system. One example is given in Fig. 2.5 and shows a coordinate system based on the azimuth-over-elevation positioner. Each of the three spherical systems has two poles. They occur when the pointing of the AUT does not change when one of the angles is varied. For the azimuth-over-elevation positioner in Fig. 2.5 the poles are located along the y-axis [18].

Like stated previously, two angles are needed to fully characterize the orientation of the AUT. The first angle (ang_1) is measured relative to the axis, on which the poles are placed and forms a circle cutting though the poles. The second angle (ang_2) describes the movement around the pole. In Fig. 2.6 the arrangement is visualized.

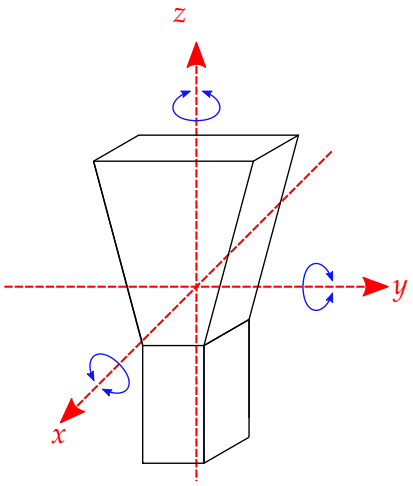

Fig. 2.4: The three degrees of freedom of rotation, visualized by a horn antenna.

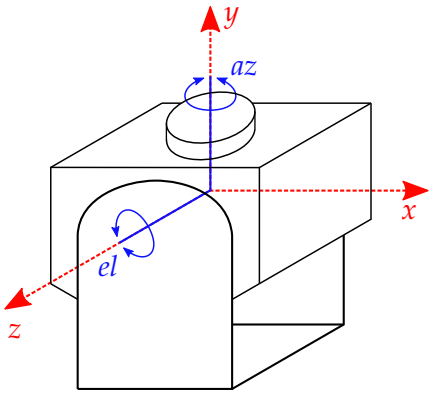

Fig. 2.5: An azimuth-over-elevation positioner, where the AUT is placed on top of it, adapted from [18].

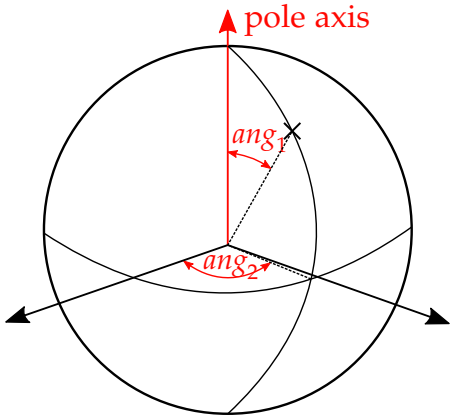

Fig. 2.6: The principle behind all three spherical coordinate systems.

In addition to the azimuth-over-elevation positioner the other two possible coordinate systems are the elevation-over-azimuth system and the roll-over-azimuth system. Tab. 2.1 shows how the different coordinate systems are related to the general definition in Fig. 2.6 [18].

The distinction between different positioner configurations is important, since the chosen configuration directly affects the obtained radiation patterns. In [18] the differences in the obtained data is shown graphically, by scanning the earths surface with different positioner configurations. Additionally the transformations, which change from one coordinate system to another, are presented in [18].

Table 2.1: The three different spherical coordinate systems in antenna measurement and their relation to the definitions in Fig. 2.6 [18]

coordinate system	pole axis	ang_1	ang_2
roll-over-azimuth	z-axis	θ	ϕ
azimuth-over-elevation	y-axis	elevation (el_1)	azimuth (az_1)
elevation-over-azimuth	x-axis	azimuth (az_2)	elevation (el_2)

2.2.2 Measurement with Polarization Characteristic

This section extends the previous discussion by adding a polarization sensitive AUT, which, in practice, is always the case. The measured pattern is a function of the polarization of the illuminating plane wave. At least two different orthogonal polarization states, called polarization bases, of the plane wave are required to completely describe the AUT. Out of these two measurements, where amplitude and phase are obtained, any polarization can be synthesized [16, p. 699][18].

In [17] three different definitions for polarization bases are made. The first set is based on Cartesian coordinates (Ludwig I), the second are the previously discussed spherical coordinates (Ludwig II) and the third definition is based on a more sophisticated positioning system called Ludwig III. It is evident that the polarization basis vectors of one system should be orthogonal to each other and normalized [16, pp. 698][17].

The first set of polarization bases are the unit vectors of a Cartesian coordinate system. According to [16, p. 700] this definition is valid in near field as well as in far field. Since the AUT is placed on a rotary positioning system, the received electric field can have components in all three Cartesian dimensions. An illustration is found in Fig. 2.7, showing the sphere, the rotated AUT describes, and exemplary the polarization bases at different locations.

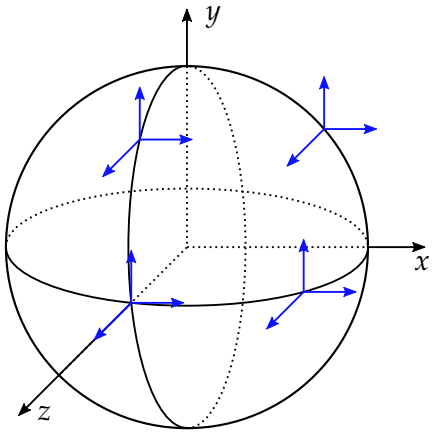

Fig. 2.7: The polarization bases aligned with a Cartesian coordinate system. The orientation is plotted on the infinite sphere, for some locations is shown in blue [16, p. 701].

The mathematical treatment is shown in the following. The electric field $\vec{E}(t,x,y,z)$ of a time harmonic wave can be described like [14, pp. 50]

$$\vec{E}(t,\vec{r}) = \mathrm{Re}\left(\vec{E}(\vec{r})\mathrm{e}^{\mathrm{j}\omega t}\right) . \tag{2.2}$$

Giving (2.2) the electric field is completely defined by the complex valued, time independent phasor $\vec{E}(\vec{r})$. For time convention $\mathrm{e}^{\mathrm{j}\omega t}$ is used and Re denotes the real part. In case of Cartesian basis vectors the phasor, $\vec{E}(\vec{r})$, in (2.2) has to be extended like

$$\vec{E}(\vec{r}) = E_x(\vec{r})\vec{e}_x + E_y(\vec{r})\vec{e}_y + E_z(\vec{r})\vec{e}_z . \tag{2.3}$$

The complex factors E_x, E_y and E_z depend on the kind of polarization (linear, elliptical etc.). The unit vectors, $\vec{e}_x$, $\vec{e}_y$ and $\vec{e}_z$, denote the polarization bases [18].

Since in antenna measurement the geometry is spherical, it is more convenient to use spherical coordinates for polarization bases. An advantage is that the radial component of the electric field is zero in far field and the polarization is fully described on basis of two angular unit vectors. As previously seen, there exist three different spherical coordinate systems, depending on the structure of the positioner. Therefore, three sets of polarization bases exist. For the azimuth-over-elevation positioner the unit vectors are shown exemplary in Fig. 2.8, marked in blue. The red lines illustrate the orientation of the basis vectors along the sphere [16, pp. 700][18].

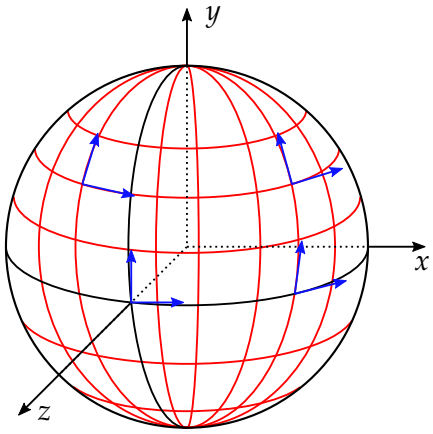

Fig. 2.8: A visualization of the spherical coordinate system based on an azimuth-over-elevation positioner. The blue colored arrows represent the unit vectors at randomly chosen positions. The red colored lines show the orientation of the basis vectors over the sphere [16, p. 706].

Along the y-axis there are two poles, leading to a soft singularity in the polarization bases. This causes problems defining the polarization in these particular directions. The problem can be solved by different techniques, which will be explained later. Utilizing an azimuth-over-elevation positioner, allows to decompose the electric field phasor from (2.2) as

$$\vec{E}(\vec{r}) = E_{az_1}(\vec{r})\vec{e}_{az_1} + E_{el_1}(\vec{r})\vec{e}_{el_1}\,. \tag{2.4}$$

Again, the factors E_{az_1} and E_{el_1} are complex values and describe the type of polarization. The suffix $_1$ is used to prevent confusion with the elevation-over-azimuth system, because the unit vectors are not the same.

A second spherical coordinate system is the elevation-over-azimuth positioning system, where the electric field phasor $\vec{E}(\vec{r})$ is expressed like,

$$\vec{E}(\vec{r}) = E_{az_2}(\vec{r})\vec{e}_{az_2} + E_{el_2}(\vec{r})\vec{e}_{el_2}\,. \tag{2.5}$$

The basis vectors are denoted as $\vec{e}_{az_2}$ and $\vec{e}_{el_2}$. In this coordinate system the poles lie along the x-axis. This explains why the basis vectors generally do not have the same orientation as $\vec{e}_{az_1}$ and $\vec{e}_{el_1}$ (azimuth-over-elevation positioner). The existence of this poles can again cause problems resolving the polarization along x-direction.

In a roll-over-azimuth system the polarization bases are $\vec{e}_\theta$ and $\vec{e}_\phi$. The corresponding phasor can be decomposed as

$$\vec{E}(\vec{r}) = E_\theta(\vec{r})\vec{e}_\theta + E_\phi(\vec{r})\vec{e}_\phi\,. \tag{2.6}$$

Usually in antenna measurement the boresight direction of the AUT is chosen to point towards z-direction. Since in a θ-ϕ system the poles are aligned with the z-axis, the singularity in the polarization basis is located in this important orientation. Without any additional techniques, which deal with the singularity, the roll-over-azimuth system is not a convenient solution [18].

A possibility to avoid the singularity in positive z-direction is to use an alternative coordinate system based on the third definition in [17], also known as Ludwig III coordinates. In this arrangement the feed is mounted on an additional rotation stage, ensuring that the feed and the AUT always remain polarization matched during the rotation along the ϕ angle. This rotation of the feed results, from a mathematical point of view, in removing the pole on the positive z-axis. The direction of the polarization bases is illustrated in Fig. 2.9 on the surface of a sphere. The blue arrows show the direction of them in some arbitrarily chosen locations. The pole on the negative z-axis can not be removed, but in most cases the polarization in that direction is not of interest [17][18].

In the literature (like [16, pp. 710]) the polarization in Ludwig III is resolved in co- and cross-polar direction. Therefore, the electric field phasor is decomposed as

$$\vec{E}(\vec{r}) = E_{\mathrm{co}}(\vec{r})\vec{e}_{\mathrm{co}} + E_{\mathrm{cross}}(\vec{r})\vec{e}_{\mathrm{cross}}\,. \tag{2.7}$$

The co-polar direction is denoted by $\vec{e}_{\mathrm{co}}$, while $\vec{e}_{\mathrm{cross}}$ is the unit vector pointing in cross-polar direction. Mathematically the rotation of the feed, leading from the roll-over-azimuth system to a Ludwig III coordinate system, is performed by the transformation

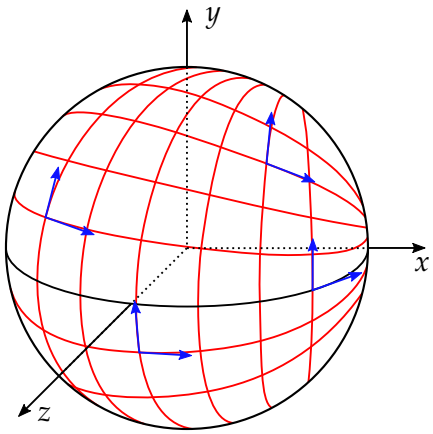

Fig. 2.9: A visualization of the polarization reference vectors (in blue color) in a coordinate system based on Ludwig III. The red colored lines represent the direction around the infinite sphere [16, p. 711].

$$\begin{pmatrix} E_{\text{co}}(\theta,\phi) \\ E_{\text{cross}}(\theta,\phi) \end{pmatrix} = \begin{bmatrix} \cos(\phi) & -\sin(\phi) \\ \sin(\phi) & \cos(\phi) \end{bmatrix} \begin{pmatrix} E_\theta(\theta,\phi) \\ E_\phi(\theta,\phi) \end{pmatrix} . \tag{2.8}$$

This transformation is only valid if a linear polarization is considered. The treatment of the more general elliptical case, leads to complex prefactors in the transformation matrix, in (2.8). A more detailed view is found in [12, pp. 215]. Similar as for the transformation matrix in (2.8), there exist also transformations from one representation to another one, they can be found in the corresponding literature [16, pp. 716].

2.3 Compact Antenna Test Ranges

In the previous section it was assumed that the AUT is illuminated by a plane wave and therefore, far field conditions apply. The generation of a locally plane wave is not trivial, and different methods, so called antenna ranges, were developed.

One method, which ensures the correct field distribution is a CATR. This antenna range is presented comprehensive in the following separate section, since an extensive part of this work regards antenna measurements in CATRs. In order to have a consistent nomenclature: A CATR is a measurement range capable of obtaining antenna parameter. The compact range at the DLR can additionally perform measurements of the Radar Cross Section (RCS) and is called a CTR.

In principle a CATR is a large reflector antenna, optimized to have a constant amplitude and phase of the near field in the aperture. A second reflector can be used, to increase the performance. The process of generating locally plane waves is called collimation. The area in the CATR, where plane wave conditions appear and therefore, the AUT is placed, is called Quiet Zone (QZ). The key advantage of CATRs is that they

have a significant smaller size than far field ranges, so they can be placed in an anechoic chamber. Interference from outside are minimized by that [10, pp. 986][13, p. 570].

The function principle of a single reflector CATR is illustrated in Fig. 2.10, by a simplified Geometrical Optics (GO) approach. In a first assumption the rays in the main beam of the feed have their origin in one point, the phase center of the feed. If the phase center is placed in the focus of the parabolic reflector, all rays reaching the QZ have the same length, leading to a wave with uniform phase [10, p. 986].

2.3.1 Compact Antenna Test Range Designs

The first CATR was build by Richard Johnson at the Georgia Institute of Technology in 1969 [6]. Since then different optimizations led to a variety of CTR types. In [6] the advantages and drawbacks of the three most often used types are discussed and analyzed numerically.

Single Reflector Compact Antenna Test Range

In Fig. 2.10 the principle of a single reflector CATR is shown. The feed antenna illuminates a paraboloidal (double curved) reflector under an offset angle. This avoids blockage and scattering of the generated plane wave. The drawbacks of this design are the high manufacturing costs of the paraboloidal reflector. Additionally this design leads to an increased cross-polarization level of wave as a consequence of the offset and the reflection. This effect is called depolarization and is inversely proportional to the focal length of the reflector [6][10, p. 989].

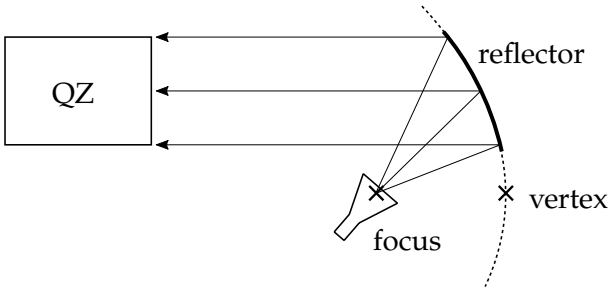

Fig. 2.10: Principle of a single reflector CTR based on the GO approximations [10, p. 986].

Dual Cylindrical Parabolic Compact Antenna Test Range

This type of CATR uses two single curved, cylindrical, parabolic reflectors to collimate the feed wave. One reflector is curved in one plane, and the second reflector is bend in the orthogonal plane. In a good approximation the wave propagating from the feed to the first reflector has spherical phase fronts. The first reflection transforms it into a cylindrical wave and the second reflector completes the collimation into a locally

plane wave. The manufacturing of a single curved parabolic cylinder is less complex and therefore, this type of CATRs is usually cheaper. The disadvantage is the same depolarization effect as for the single reflector CATR [6][10, p. 990].

Compensated Compact Antenna Test Range

The compensated CATR principle consists of two double curved reflectors. The sub-reflector has a hyperbolic form and ensures an ideal illumination of the parabolic main-reflector and guarantees a high illumination efficiency. The main advantage is the very low cross-polarization of the generated plane wave in the QZ. This comes at the cost of high manufacturing expenses, because two paraboloidal reflectors must be manufactured [6][10, pp. 990][19].

The essential groundwork for the principle is given in [20]. The cross-polarized component, generated by the offset geometry of the main-reflector, is canceled by a proper arrangement of the hyperbolic shaped sub-reflector. The so called Mizuguchi condition [8], for minimizing the cross-polarization level, is

$$\tan(\alpha) = \frac{|1 - e_{\text{sub}}^2| \sin(\beta)}{(1 + e_{\text{sub}}^2) cos(\beta) - 2e_{\text{sub}}}\,. \tag{2.9}$$

The angle between horn axis and the rotation axis of the sub-reflector is called α. The angle between the two rotation axes of both reflectors is denoted by β and e_{sub} stands for the eccentricity of the sub-reflector. In [20, p. 4] the geometrical arrangement is shown in Fig. 1.

2.3.2 Compact Antenna Test Range Error Sources

Each type of CATRs has technical limitations, which leads to the fact that the generated wave is only an approximation of a plane wave. Therefore, in the context of CATRs, a locally plane wave is defined in most cases by a phase error of less than 10° peak to peak, and an amplitude deviation of $\pm 0.5\,\text{dB}$ [10, p. 987].

Diffractions

One source of errors are the diffractions at the edges of the reflector. The strong discontinuity causes fields, which interfere with the reflected wave in the QZ and generate ripples in amplitude and phase of the plane wave. In order to weaken this problem, different edge treatments are developed. Their basic idea is to form a smooth transition from the sharp discontinuity between reflector and free space. This can be done by curving the edges towards the back of the reflector, and is called rolled edge treatment and is visualized in Fig. 2.12. Another possibility is to use serrations, see Fig. 2.11. Their shape leads to a tapering of the reflected wave at the edge of the reflector. Therefore, due to the large number of serrations multiple diffractions are

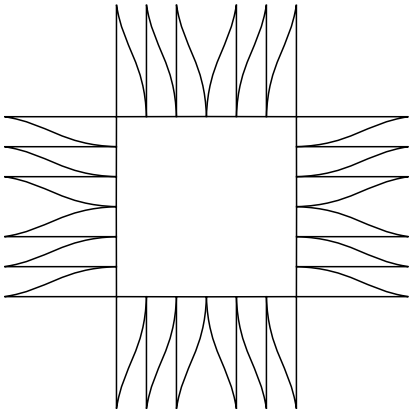

Fig. 2.11: A reflector with serrations in front view, like used in the CTR of the DLR adapted from [10, p. 988].

Fig. 2.12: Curved edge treatment to avoid diffractions, taken from [10, p. 988] in side view.

generated, having a significant lower amplitude than a sharp edge. The shape of them can vary from simple triangular to more complex curves, like cosine functions, leading to a better performance at higher frequencies. Other edge treatments use feeds with a particular radiation pattern, which do not illuminate the edges. As an alternative the field at the edges can be tapered by using absorbing materials [10, pp. 987].

Field Tapering

Additionally to the ripples in amplitude and phase, the amplitude in the QZ can have a tapering. This discrepancy of the ideal plane wave has two origins: The shape of the feed pattern has an influence on the fields in the QZ. The higher the directivity of the feed, the larger gets the amplitude tapering, because the feed pattern is directly mapped into the QZ. Therefore, in most CATRs low gain feeds are used to minimize it [10, p. 987].

The second effect causing the tapering in the amplitude is the free space attenuation. All ray path lengths from the feed to the QZ have the same length, but the distance from the feed to the reflector varies with the angle, see Fig. 2.10. The difference in the path length results in a different field strength at the reflector due to the $1/r^2$ attenuation. This tapering is unsymmetrical, which can be seen in the co-polar field plots in Section 4 [10, p. 987].

Frequency Limitation

An important limitation is the shape and size of the reflectors, both define the highest and lowest usable frequency. The lower frequency limit is reached when the reflector's diameter is about 25λ to 30λ. Where λ is the wavelength of the wave. At high frequencies the finite surface precision of the reflector has to be considered. The upper

limit is reached, when the surface deviates more than 0.007λ from the ideal paraboloid. For dual reflector CATRs the surface precision has to be two times higher [10, p. 989].

Cross-Polarization

Ideally a CTR would have an ideal polarized plane wave in the QZ, without any cross-polarization component. The depolarization of offset reflector antennas is analytically discussed in [4]. All obtained results in [4] apply directly for paraboloidal, single reflector CATRs. It is shown that for a circularly symmetric feed pattern, feeding centrally a parabolic reflector, no cross-polarization occurs. To avoid blockage, CATRs always have an offset geometry. This offset angle between the feed axis and the reflector axis causes a depolarization of the reflected electric field. The cross-polarization is distributed in the aperture in a distinct way. Along the symmetry plane no depolarization occurs but it increases towards the edges of the aperture. A minimization of the cross-polarization can be achieved by reducing the offset angle and increasing the focal length [4].

The cross-polarization performance of dual cylindrical parabolic CATRs is analyzed in [5]. The influence of the geometry is extensively discussed and the most important findings are summarized: The angle between feed axis and sub-reflector has the same influence as the offset angle in single reflector systems. In general both reflectors have different focal lengths and increasing them, reduces the cross-polarization. The main-reflector's focal length has more influence compared to the sub-reflector. Assuming a rotationally symmetric feed pattern, the cross-polarization performance of the CATR is nearly independent from the feed pattern [5].

2.3.3 The Compact Test Range at the German Aerospace Center

At the Microwaves and Radar Institute at the DLR, a dual cylindrical parabolic CTR is used to perform antenna measurements and RCS analysis. It was build by March Microwave System B.V. and has the model number 8074B. A picture of the chamber is shown in Fig. 2.13. According to the specifications in [21] the CTR can be used over a frequency range from 1 GHz to 100 GHz. The chamber dimensions are about 24 m in length and 11.7 m in width. About 10 m is the height. Both cylindrical parabolic reflectors consist of aluminum sheets. The requirements to the surface accuracy are very high. Therefore the aluminum is glued on a honeycomb structure, avoiding a deformation under its own weight.

An illustration of the function principle and the reference coordinate system is shown in Fig. 2.14. The sub-reflector is curved in the xy-plane, while the curvature of the main-reflector is in the xz-plane. Since both are orthogonal the spherical wave of the feed is collimated into a locally plane wave. In Fig. 2.13 the sub-reflector is shown in the left. Its dimensions are 2.9 m and 3.8 m in height, without the serrations. The sub-reflectors shape is a symmetrical parabolic cylinder, meaning the apex is in the center line of the mirror. The main-reflector has a length of 4.7 m and a width of

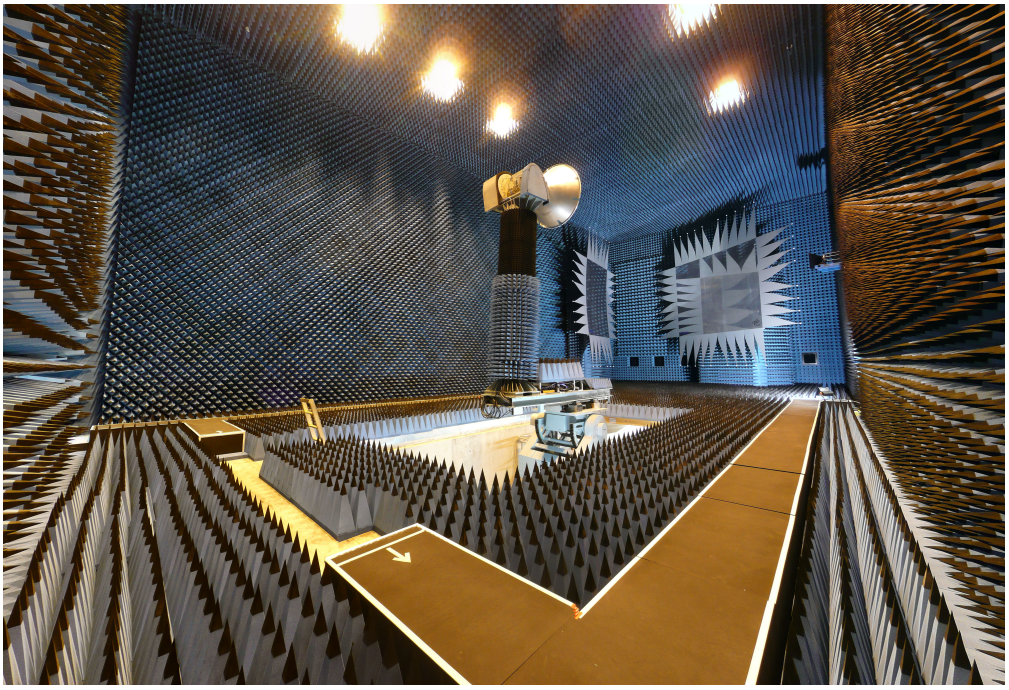

Fig. 2.13: The CTR at the Microwaves and Radar Institute at the DLR.

3.8 m. In contrast to the sub-reflector its shape is an unsymmetrical cut of a cylindrical paraboloid. The size of both reflectors leads to a QZ of 3 m in diameter at 1 GHz. With higher frequencies the diameter increases to 3.6 m. Additionally to the errors explained in Section 2.3.2, three more imperfections sources must be considered.

It can be seen in Fig. 2.14, that a side lobe of the feed can illuminate directly the QZ. This is shown by the dashed blue colored line. Since the path length of the direct illumination is significantly shorter than the path including the two reflections, it can be corrected by using time-gating. Therefore, at the DLR a frequency chirp is used for the transmit signal and the time-gating is processed based on the chirp z-transformation.

The walls, ceiling and floor of the measurement chamber are covered with pyramidal absorbers. But this materials do not perfectly absorb an incoming wave. The reflection coefficient strongly depends on the angle of incidence therefore, the influence of this reflections is difficult to predict. A solution is to use high quality absorbers with a low reflection coefficient.

The ideal ray path (marked as red colored arrow in Fig. 2.14) is first reflected at the sub-reflector and then at the main-reflector. The feed is also illuminating the main-reflector, leading to an unwanted ray path with three reflections (marked by the continuous blue arrow). In practical measurements it is not possible to suppress this triple reflections by time-gating. One possibility to avoid tripe reflections is to design the feed, in a way that the radiation in direction of the main-reflector is minimized. At

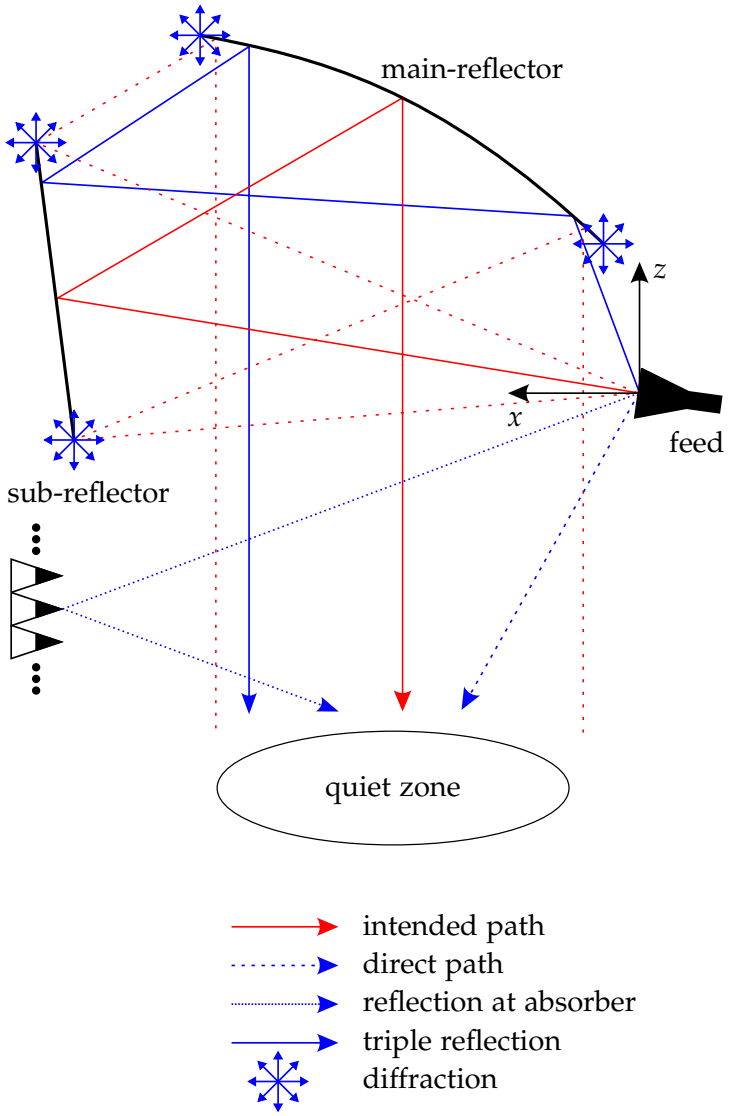

Fig. 2.14: Principle of the CTR at the DLR with two reflectors, including the different error sources [21].

the DLR all feed antennas are placed inside of a conical impedance wall, like shown in the appendix A.1. It minimizes the direct illumination of the main-reflector and reduced the effect of the triple reflections. In [19] an alternative improvement is presented, by placing a cylindrical structure covered with absorbers is between the feed and the main-reflector.

In Section 2.1 different positioning systems and their influence on the polarization bases is discussed. Therefore, a special focus is on the positioning system of the CTR. Considering the coordinate system in Fig. 2.14 the position of it is at $x = 4.0\,\mathrm{m}$, $y = 0\,\mathrm{m}$ and $z = -9.5\,\mathrm{m}$.

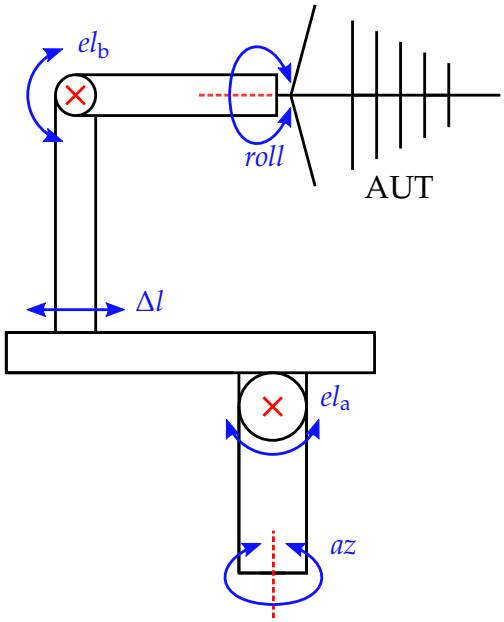

Fig. 2.15: The principle of the positioning system in the CTR at the DLR. Possible rotation and translation movements are marked in blue color [21].

The principle of the positioning system is illustrated in Fig. 2.15. It consists of four rotation points and one linear axis. The actual pattern measurement is mostly done in a roll-over-azimuth configuration (see Section 2.1), for this the rotation around *roll* and *az* is needed. Measurements in other configurations can be done as well, but the standard at the institute is roll-over-azimuth. In case the AUT is large and heavy, a rotation around the angles el_a and el_b allows a more comfortable access to the mounting plate. The translation movement along Δl is used to place the AUT over the rotation axis of the azimuth angle. This is important to have a fixed reference around the AUT is turned, essential for the evaluation of the phase center [21].

2.3.4 Further Types of Antenna Ranges

For completeness the following section describes the different antenna ranges briefly. This includes their function principle as well as the individual advantages and disadvantages.

Far Field Ranges

The idea behind far field ranges is, like the name suggests, to place the AUT in the far field of the feed. A sufficiently large distance between the antennas must be ensured that the received wave has planar phase fronts. In many systems both antennas are mounted on towers. This arrangement is usually low cost, but due to the

potentially large dimensions, far field ranges are often build outside. This makes the measurement dependent on the weather, and natural or man made noise can corrupt the measurements [13, pp. 566]. The dynamic range of far field ranges is typically lower, because of the free space attenuation.

Reflection Ranges

In far field ranges the reflection of the wave at the ground is not wanted, instead in reflection ranges it is desired. The feed and the AUT are both mounted on lower height, so that the direct line of sight and the reflected path have nearly the same length. This results in a constructive interference and the phase variation in the measuring zone is small. The lower position of the AUT makes reflection ranges convenient for measurements of large antennas, like full size aircraft or satellites. The disadvantages are similar as for far field ranges [13, pp. 571].

Near Field to Far Field Techniques

One way to perform antenna measurement in smaller test ranges, and reducing the costs, is applying a NF/FF transformation. The AUT is placed in the near field of the feed antenna and operates in transmitting mode. Due to their smaller size they can be used indoor in anechoic chambers, in a well controlled environment. The feed antenna (in this case called field probe) is moved in order to gather different samples, which consist of the magnitude and the phase of the received electric field. The movement can be done on a well defined surface, e.g. on a cylinder or a sphere. It is also possible to use an arbitrary surface and an irregular sampling grid. This can decrease the computational time significantly [10, pp. 992][22].

In order to get far field data, the measured near field samples have to be processed by a NF/FF transformation algorithm. The principle behind is the Fourier transformation. Dependent on the surface, on which the near field samples are located, additional processing steps have to be included. The post processing also includes probe corrections and calibration techniques. This computational effort leads to expensive and sophisticated software and elaborate calibration principles. Also the positioning systems can be complex and expensive. An additional drawback is that the field probe is in the near field of the AUT and interferes with it [13, p. 570][23].

2.4 Numerical Optimization

Numerical optimization, also called programming, is an important topic not only in mathematics, also in natural science, engineering or economics. This section gives a compact overview, focusing on nonlinear optimization. First the general topic of numerical optimization and the basic concept is presented. A small part discusses linear programming, which is extended to nonlinear optimization in the last part.

2.4.1 Basic Concept

The following consideration is limited to finite dimensional and continuous optimization problems. They are written in the form

$$\begin{aligned} \min \quad & f(\boldsymbol{x}) \\ \text{s.t.} \quad & \boldsymbol{x} \in X\,. \end{aligned} \tag{2.10}$$

The objective function is denoted by $f(\boldsymbol{x})$, and the vector $\boldsymbol{x}$ is n-dimensional, containing all unknowns. The optimization problem in (2.10) has the side constraint, that $\boldsymbol{x}$ must be an element of the set X. A maximization problem is described analog by negating $f(\boldsymbol{x})$ and solving the minimization [24, pp. 1].

A local minima, $\boldsymbol{x}_{\min}$, is defined by

$$f(\boldsymbol{x}_{\min}) \leq f(\boldsymbol{x}) \qquad \text{for all} \qquad \boldsymbol{x} \in X \cap B_\epsilon(\boldsymbol{x}_{\min})\,. \tag{2.11}$$

$B_\epsilon(\boldsymbol{x}_{\min})$ is a n-dimensional sphere defined by $B_\epsilon(\boldsymbol{x}_{\min}) = \{\boldsymbol{x} \in \mathbb{R}^n : \|\boldsymbol{x} - \boldsymbol{x}_{\min}\| < \epsilon\}$. It is a multidimensional sphere centered at the local minima with arbitrarily small radius smaller than ϵ. If $\boldsymbol{x}_{\min}$ minimizes the objective function on entire X, it is called a global minimum.

The search for a global optimum can get highly complex, even for low dimensional problems. There exists a variety of different algorithms for such global optimization tasks, like evolutionary algorithms, neuronal networks, simulated annealing, stochastic simulations and many others. A discussion of global optimization is not scope of this, in the following pages only methods searching for local minima are discussed. The results of these algorithms strongly depend on the stating point, which is chosen by the user. A priori knowledge must be available, to find a physically meaningful starting point, which ensures convergence towards the correct minimum [25, pp. XIV].

Optimization tasks can be divided in two parts, constraint and unconstrained problems. If in (2.10) the set $X = \mathbb{R}^n$, the optimization is unconstrained. For constraint problems it is assumed that the set X can be described by a system of equations and inequations. This assumption has no significant limitations for practical applications. The set X is defined as

$$X = \{\boldsymbol{x} \in \mathbb{R}^n : \boldsymbol{h}(\boldsymbol{x}) = 0, \boldsymbol{g}(\boldsymbol{x}) \leq 0\}\,. \tag{2.12}$$

Where the inequality, $\boldsymbol{g}(\boldsymbol{x})$ is considered to be component wise. If the objective function $f(\boldsymbol{x})$ and $\boldsymbol{g}(\boldsymbol{x})$ are convex and additionally $\boldsymbol{h}(\boldsymbol{x})$ is linear, the underlying optimization problem is called convex. This property implies that each local minimum is also a global minimum [24, p. 3].

2.4.2 Linear Programming

Linear optimization is a special case of the previous presented general problem statement. All functions $f(\boldsymbol{x})$, $\boldsymbol{h}(\boldsymbol{x})$ and $\boldsymbol{g}(\boldsymbol{x})$ are linear, meaning they can be rewritten

like

$$\begin{aligned} f(\boldsymbol{x}) &= \boldsymbol{c}^{\mathrm{T}}\boldsymbol{x} \\ \boldsymbol{h}(\boldsymbol{x}) &= \boldsymbol{B}\boldsymbol{x} - \boldsymbol{d} \\ g(\boldsymbol{x}) &= \boldsymbol{A}\boldsymbol{x} - \boldsymbol{b}\,. \end{aligned} \tag{2.13}$$

Where $\boldsymbol{A}$ and $\boldsymbol{B}$ are matrices, the vectors are $\boldsymbol{b}$, $\boldsymbol{c}$ and $\boldsymbol{d}$. Since linear functions are convex (and also concave) linear programming problems are convex, having the advantage described above [24, p. 2]. Besides (2.13) other problem statements are possible. One example is the so called canonical form

$$\begin{aligned} \min \quad & \boldsymbol{c}^{\mathrm{T}}\boldsymbol{x} \\ \text{s.t.} \quad & \boldsymbol{A}\boldsymbol{x} \leq \boldsymbol{b}\,. \end{aligned} \tag{2.14}$$

All forms are fully equivalent and can be converted into each other [26, pp. 9].

The side constraint in the canonical form allows a geometrical interpretation: A polyhedron $P(\boldsymbol{A}, \boldsymbol{b})$ is mathematically described by $P(\boldsymbol{A}, \boldsymbol{b}) = \{\, \boldsymbol{x} \in \mathbb{R}^n : \boldsymbol{A}\boldsymbol{x} \leq \boldsymbol{b}\}$, which is the same definition as for $\boldsymbol{x}$ in (2.14). Depending on $P(\boldsymbol{A}, \boldsymbol{b})$ three cases are possible, which affect the solubility of the linear programming problem [26, pp. 57][27, pp. 13]:

1. The system $\boldsymbol{A}\boldsymbol{x} \leq \boldsymbol{b}$ has no solution, meaning the at least two rows of the equation system are contradicting each other. This corresponds to an empty polyhedron, and the optimization can not be done.

2. The polyhedron is not constraint, mathematically speaking $\forall \mathbf{p} \in P : \|\mathbf{p}\| \not< M$. Where M is an arbitrarily large real number. The optimization problem is not constraint and has an infinite number of solutions.

3. If the polyhedron is constraint and not empty, at least one minimum (and maximum) can be found during the optimization.

It is evident that the third case is most relevant for practical applications. In [26, pp. 96] the following important statement is made and proven. If the polyhedron $P(\boldsymbol{A}, \boldsymbol{b})$ is not empty and $\boldsymbol{A}$ has full column rank, the optimum of the objective function $f(\boldsymbol{x}) = \boldsymbol{c}^{\mathrm{T}}\boldsymbol{x}$ must be located in a vertex of the polyhedron. This is valid only if $f(\boldsymbol{x})$ is constraint on $P(\boldsymbol{A}, \boldsymbol{b})$.

The geometrical consideration of the linear programming gives a good visualization of the solving methods. In the following two algorithms are briefly presented, a mathematically more comprehensive treatment is found in [26, pp. 95, 207].

Simplex Algorithm

The simplex algorithm is an iterative procedure. Starting from a vertex of the polyhedron all neighboring vertices are analyzed if one of them diminishes the result

of the objective function. Than the procedure starts from this vertex again, until no further decrease is possible. The local optimum is found, and given the fact that linear programming problems are convex, it coincides with the global optimum. Considering the polyhedron, the simplex algorithm iterates along the outer edges from one vertex to another [26, pp. 95].

To determine the vertices of the polyhedron mathematically, the concept of a basis is introduced. The set $B \subseteq \{1, \ldots, n\}$ is called basis if the so build submatrix $\boldsymbol{A}_{.B}$ is regular. $\boldsymbol{A}_{.B}$ is constructed by taking the rows of $\boldsymbol{A}$ indexed by the set B. The complementary set N is defined by $\{1, \ldots, n\} \setminus B$. The vector $\boldsymbol{x} \in \mathbb{R}^n$ is constructed by $(\boldsymbol{x}_B, \boldsymbol{x}_N)$. It is called a basic feasible solution when

$$\boldsymbol{x}_B = \boldsymbol{A}_{.B}^{-1}\boldsymbol{b} \qquad \text{and} \qquad \boldsymbol{x}_N = 0\,. \tag{2.15}$$

It is shown that each basic feasible solution is a vertex of the polyhedron.

To determine if a neighboring vertex $\boldsymbol{x}_{\text{next}}$ is an improvement, first the gradient of the objective function is analyzed. Since $f(\boldsymbol{x})$ is linear, the gradient is $\boldsymbol{c}^{\mathrm{T}}$. In the next step the direction vector $\boldsymbol{d}$ from the start vertex to $\boldsymbol{x}_{\text{next}}$ is calculated. The angle between the gradient and the direction vector can be calculated by applying the scalar product. In a minimization problem $\boldsymbol{c}^{\mathrm{T}}\boldsymbol{d}$ must be smaller than zero to further improve the path. If at some vertex $\boldsymbol{c}^{\mathrm{T}}\boldsymbol{d} \geq 0$ for all possible $\boldsymbol{d}$ the global minimum is found to be at this vertex [26, pp. 99].

Interior Point Methods

The name interior points covers multiple solving methods. Known from the theory of linear programming, the optimum is located at a vertex of the polyhedron. In contrast to the simplex algorithm, interior points methods iterate towards the optimum, through the inside of the polyhedron. In order to prevent the algorithm from reaching the surface, two different principles are developed. One way is to use barrier and penalty functions. They punish the way towards the surface, by manipulating the objective function.

An other way is to use a transformation, which manipulates the polyhedron so that the current iteration point is at its center. A step towards the gradient ($\nabla f(\boldsymbol{x}) = \boldsymbol{c}$, for linear functions) is made and the solution is transformed back. This procedure is repeated iteratively until the optimum is found. The first developed interior point algorithm, named after its inventor, is the Karmarkar method. It uses penalty functions, and the transformation principle. It is presented in the following [26, pp. 207].

Any linear programming problem can be transferred in to the Karmarkar normal form,

$$\begin{aligned} \min \quad & \boldsymbol{c}^{\mathrm{T}}\boldsymbol{x} \\ \text{s.t.} \quad & \boldsymbol{A}\boldsymbol{x} = 0\,, \\ & \boldsymbol{e}^{\mathrm{T}}\boldsymbol{x} = 1\,, \\ & \boldsymbol{x} \geq 0\,, \end{aligned} \tag{2.16}$$

which is essential to apply the solving algorithm. The vector $\boldsymbol{e}^{\mathrm{T}} = (1, \ldots, 1)$ can have different length. It is so defined that the corresponding matrix vector and vector vector products are possible. The matrix $\boldsymbol{A}$ must have full rank and $\boldsymbol{A}\boldsymbol{e} = 0$. In the Karmarkar algorithm only a part of the polyhedron is transformed, the unit simplex. It is defined as

$$\Delta = \{\boldsymbol{x} \in \mathbb{R}^n_+ : \boldsymbol{e}^{\mathrm{T}}\boldsymbol{x} = 1\}\,. \tag{2.17}$$

The center point of the unit simplex is $\boldsymbol{c}_\Delta = (1/n)\boldsymbol{e}$. It is known that the radius of the inscribed sphere of a unit simplex is $r = 1/\sqrt{n(n-1)}$. For all points inside of Δ a transformation, $\pi_{\boldsymbol{x}}(\boldsymbol{y})$ is defined, which projects $\boldsymbol{x}$ on the center $\boldsymbol{c}_\Delta$. The vertexes of the simplex are not transformed. The transformation is calculated via [26, p. 210]

$$\pi_{\boldsymbol{x}}(\boldsymbol{y}) = \frac{\boldsymbol{X}^{-1}\boldsymbol{y}}{\boldsymbol{e}^{\mathrm{T}}\boldsymbol{X}^{-1}\boldsymbol{y}} \qquad \text{respective} \qquad \pi^{-1}_{\boldsymbol{x}}(\boldsymbol{y}) = \frac{\boldsymbol{X}\boldsymbol{y}}{\boldsymbol{e}^{\mathrm{T}}\boldsymbol{X}\boldsymbol{y}}\,. \tag{2.18}$$

The matrix $\boldsymbol{x}$ is quadratic and has the entries of $\boldsymbol{x}$ on the main diagonal. Starting from (2.17) and (2.18) the algorithm can be constructed:

The current iteration point, $\boldsymbol{x}$ is transformed by (2.18) on the center point c_Δ. From that a step along the transformed negative gradient is taken. The maximum length of the step could be r, but in order to stay sufficiently away from the surface the maximum step size is scaled by $\varsigma \in]0, 1[$. The so obtained point is transformed back by $\pi^{-1}_{\boldsymbol{x}}(\boldsymbol{y})$ and the iteration starts again [26, pp. 210].

Usually the algorithm converges and stops when a lower boundary of ε is reached. It is important to state that the gradient of objective function must also be transformed by (2.18), this can cause problems, because non linearities occur [26, p. 211].

2.4.3 Nonlinear Programming

Starting from the most general case in (2.10) the nonlinear programming problem is rewritten like [24, p. 3]

$$\begin{aligned} \min \quad & f(\boldsymbol{x}) \\ \text{s.t.} \quad & \boldsymbol{h}(\boldsymbol{x}) = 0\,, \\ & \boldsymbol{g}(\boldsymbol{x}) \leq 0\,. \end{aligned} \tag{2.19}$$

Like previously discussed the functions $\boldsymbol{h}(\boldsymbol{x})$ and $\boldsymbol{g}(\boldsymbol{x})$ describe the boundaries of the problem. For unconstrained problems both are neglected. In general the minimization

problem in (2.19) is not convex. The property that each local minimum is also a global minimum, is not valid anymore [24, pp. 2].

First the optimization conditions are presented, which define what necessary and sufficiency criteria a point $\boldsymbol{x}$ must fulfill to be a local minimum. The discussion is similar to the case of one dimensional functions: Where the necessary condition is $f'(x) = 0$, and $f''(x) > 0$ is the sufficient criterion. For multidimensional problems the discussion is more lengthy. In the following only constrained nonlinear problems are considered. For unconstrained optimization the criteria are less comprehensive and can be found in [24, pp. 11].

The first order conditions are the so called Karush-Kuhn-Tucker (KKT) conditions. They describe the necessary properties a point $\boldsymbol{x}$ must have, which are according to [24, pp. 94] and [28, pp. 342]:

$$\begin{aligned} \nabla f(\boldsymbol{x}) + \boldsymbol{\lambda}^{\mathrm{T}} \nabla \boldsymbol{g}(\boldsymbol{x}) + \boldsymbol{\mu}^{\mathrm{T}} \nabla \boldsymbol{h}(\boldsymbol{x}) = 0\,, \\ \boldsymbol{h}(\boldsymbol{x}) = 0\,, \\ \boldsymbol{\lambda} \geq 0\,, \\ \boldsymbol{g}(\boldsymbol{x}) \leq 0\,, \\ \boldsymbol{\lambda}^{\mathrm{T}} \boldsymbol{g}(\boldsymbol{x}) = 0\,. \end{aligned}$$

The vectors $\boldsymbol{\lambda}$ and $\boldsymbol{\mu}$ are called Lagrange multipliers.

The second order criterion includes the so called Hessian matrix. Assuming that the function $f(\boldsymbol{x})$ is twice continuously differentiable and $\boldsymbol{x}$ is n-dimensional, the Hessian matrix $\boldsymbol{F}(\boldsymbol{x})$ has the size of n by n. Its entries are defined by

$$F_{i,j}(\boldsymbol{x}) = \frac{\partial^2 f(\boldsymbol{x})}{\partial x_i \partial x_j}\,. \tag{2.20}$$

The Hessian matrix is always symmetric, due to Schwarz's theorem [29, p. 220]. Another important concept is definiteness. A quadratic matrix $\boldsymbol{A}$ of the size n by n is called positive definite if [29, pp. 100]

$$\boldsymbol{x}^{\mathrm{T}} \boldsymbol{A} \boldsymbol{x} > 0 \quad \text{for} \quad \boldsymbol{x} \in \mathbb{R}^n\,. \tag{2.21}$$

The vector $\boldsymbol{x}$ must at least have one entry not equal to zero. The statement in (2.21) is equivalent to analyzing the eigenvalues of $\boldsymbol{A}$. If all eigenvalues are larger than zero, the matrix is positive definite. If (2.21) is smaller than zero (and all eigenvalues are smaller 0) the matrix is negative definite.

The sufficient criterion for $\boldsymbol{x}$ being a local minimum of the optimization problem in (2.19), states that the matrix $\boldsymbol{L}(\boldsymbol{x})$ must be positive definite. It is calculated by [28, pp. 344]

$$\boldsymbol{L}(\boldsymbol{x}) = \boldsymbol{F}(\boldsymbol{x}) + \boldsymbol{\lambda}^{\mathrm{T}} \boldsymbol{G}(\boldsymbol{x}) + \boldsymbol{\mu}^{\mathrm{T}} \boldsymbol{H}(\boldsymbol{x})\,. \tag{2.22}$$

Where $\boldsymbol{F}(\boldsymbol{x})$, $\boldsymbol{G}(\boldsymbol{x})$ and $\boldsymbol{H}(\boldsymbol{x})$ are Hessian matrices to the corresponding functions. The positive definiteness of $\boldsymbol{L}(\boldsymbol{x})$ must hold true on the subspace [28, pp. 344]

$$M' = \{\boldsymbol{y} : \nabla \boldsymbol{h}(\boldsymbol{x})\boldsymbol{y} = 0, \nabla g_j(\boldsymbol{x})\boldsymbol{y} = 0 \quad \forall j \in J\} \tag{2.23}$$

with

$$J = \{j : g_j(\boldsymbol{x}) = 0, \lambda_j > 0\}\,. \tag{2.24}$$

After the discussion of the KKT conditions for local minima, the solving methods for nonlinear programming are presented. Generally they can be divided in two classes depending if they solve constraint or unconstrained problems. In the following only methods for constrained optimization are discussed, in context of this work they are more important. The methods for solving unconstrained problems can be found in great detail in [24, pp. 11].

Penalty Methods

The concept of penalty functions is also used for linear programming in from of interior point algorithms. In this paragraph they are explained in more detail. The basic concept of penalty methods is to approximate the constrained problem by a unconstrained optimization. In order to do that, a penalty term is added to the objective function, which introduces high costs when the constraints are violated. The corresponding optimization problem is [24, pp. 114][28, pp. 402]

$$\min \quad f(\boldsymbol{x}) + \xi_\mathrm{p}\gamma(\boldsymbol{x})\,. \tag{2.25}$$

Where $\xi_\mathrm{p} > 0$ is the penalty parameter and $\gamma(\boldsymbol{x})$ is the penalty function. It is defined like

$$\gamma(\boldsymbol{x}) = 0 \qquad \text{for} \quad \boldsymbol{x} \in X\,,$$
$$\gamma(\boldsymbol{x}) > 0 \qquad \text{for} \quad \boldsymbol{x} \in \mathbb{R}^n_+ \setminus X\,.$$

The set X, contains all allowed values of $\boldsymbol{x}$. In literature different types of functions are presented, but most of them have a quadratic term, for the part of the unconstrained function outside of X. Additionally $\gamma(\boldsymbol{x})$ is assumed to be continuous. The correct determination of the penalty parameter, ξ_p, is not trivial. A good approximation of the solution of (2.25) with the actual constraint problem in (2.19), requires a large ξ_p. On the other hand this causes a very poor convergence of the obtained unconstrained optimization [28, pp. 401].

This problem is overcame by using the following iterative procedure [24, p. 115] [28, pp. 403]: Start the first iteration with $k = 0$ and set the penalty parameter $\xi^0_\mathrm{p} > 0$ and calculate the solution $\boldsymbol{x}^0$ of the first iteration of the penalty problem in (2.25). Since the penalty problem is only an approximation, usually $\boldsymbol{x}^\mathrm{k} \notin X$. In each consecutive

repetition $\boldsymbol{x}^k$ is used as starting point and ξ_p^k is increased. This procedure is so long repeated until $\boldsymbol{x}^k \in X$.

The unconstrained problem in (2.25) can be solved by different algorithms. Many of them are extensively discussed in [24, pp. 18] and [28, pp. 183]. Exemplary the Newton's method is briefly presented. Usually used for solving nonlinear systems of equations, it is also a prominent way to minimize functions [24, pp. 41].

Assuming that the function $f(\boldsymbol{x})$ is twice continuously differentiable. It is known that the necessary condition for a minimum is $\nabla f(\boldsymbol{x}) = 0$. From this set of nonlinear equations, with a starting point $\boldsymbol{x}^0$, the following steps are repeated [24, p. 42]: Calculate the step size $\boldsymbol{s}^k$ by solving

$$\boldsymbol{F}(\boldsymbol{x}^k)\boldsymbol{s}^k = -\nabla f(\boldsymbol{x}^k)\,. \tag{2.26}$$

In (2.26), $\boldsymbol{F}(\boldsymbol{x})$ is the Hessian matrix of the function $f(\boldsymbol{x})$, defined in (2.20). The new evaluation point is calculated via $\boldsymbol{x}^{k+1} = \boldsymbol{x}^k + \boldsymbol{s}^k$. The steps are repeated until the termination criterion of $\nabla f(\boldsymbol{x}^k) = 0$ is reached. A big advantage of the Newton's method is its fast convergence. This makes it suitable for even the problems with poor convergence properties [24, pp. 46].

Barrier Methods

Barrier methods are similar to the previously discussed penalty algorithm. The objective function of the constrained optimization is manipulated by a so called barrier function, $\psi(\boldsymbol{x})$. While in the penalty method only a concrete violation of the constrains is punished, the barrier function has a different form. It must be continuous, and $\psi(\boldsymbol{x}) \to \infty$, as $\boldsymbol{x}$ approaches the boundary of the constrained set X. Already the approaching towards the constraints is punished. Due to that property, the barrier methods can only applied to problems having inequalities, which constrain X. The corresponding, now unconstrained optimization problem

$$\min \quad f(\boldsymbol{x}) + \xi_b \psi(\boldsymbol{x})\,. \tag{2.27}$$

Where ξ_p fulfills a similar role as previously the penalty parameter. The rest of the algorithm is the same as for the penalty method [24, pp. 136]:

For each iteration the parameter ξ_b is increased. The approximated, now unconstrained, problem is solved by for example the Newton's method. This iterative procedure converges towards the optimum.

An advantage is that due to the form of $\psi(\boldsymbol{x})$ the solving algorithm always stays inside of X, if the starting point is in the interior of X. Optimization problems, like in (2.19), where the set X is constrained by inequations and equations, the interior points algorithms are extended by the penalty method [24, pp. 136].

Prominent examples for barrier functions are [28, pp. 412]:

$$\gamma(\boldsymbol{x}) = \sum_{j=1}^{p} \frac{1}{g_j(\boldsymbol{x})}$$

and

$$\gamma(\boldsymbol{x}) = -\sum_{j=1}^{p} \log(g_j(\boldsymbol{x}))\,.$$

Where $g_j(\boldsymbol{x}) > 0, j = 1, \ldots, p$ defines the set X.

3 Analysis of the CTR and Feed Development

This chapter starts with a simulative analysis regarding the depolarization of the CTR, performed in HFSS. A validation of them is done by using measured field probe data from the CTR. Based on both the compensation concept is determined and a new feed is developed. A special focus is on the numerical optimization of the weighting factors of the array elements.

3.1 Depolarization of the Compact Test Range

In the following section the depolarization of the DLR's CTR is presented. It is done in a first step by simulations. The obtained results for the cross-polar level in the QZ are compared with the theoretical findings in the corresponding literature, and with measurements.

3.1.1 Simulation Environment

All simulations are performed in Ansys EDT/HFSS 2021R2. The software supports different solving algorithms. For large scale problems the Shooting and Bouncing Rays (SBR)+ solver is suited. It is a ray tracing technique, which is combined with different correction techniques. The edge diffraction effects are considered by the Uniform Theory of Diffraction (UTD) and the Physical Theory of Diffraction (PTD). Additionally the solver simulates also creeping waves and self coupling effects [30]. To keep the computational time low, the correction techniques are not applied in most of the simulations. The simulated near fields are visualized on a grid of 601 by 551 sample points. They are located on a xy-plane at $z = -9.5\,\mathrm{m}$. The QZ has a quadratic shape of approximately 3.6 m by 3.6 m. In the plots the QZ is marked by a red colored rectangle.

The chamber geometry is found in the appendix A.11, including all relevant positions of the reflectors. Based on this document the CTR is remodeled in HFSS. Since the SBR+ solver does not support finite conductivity, the reflector models use Perfect Electric Conductor (PEC). The software gating, which is used in the CTR to suppress the direct illumination, is not supported in a single frequency domain. Instead only the scattered fields from the reflectors are visualized, having the same effect. Calculating the scattered field is only possible with the SBR+ solver, therefore other techniques like integral equation or physical optics are not considered.

In the setup of the SBR+ solver requires a correct ray density parameter. There is a direct relation between accuracy of the simulation and a higher ray density, but this also increases the computational time. The determination of the correct value is done by analyzing the convergence of the results for increasing ray density. A sufficient high accuracy is found for 0.5 rays per wavelength, the computational time is 37 h.

As feed antenna the currently used X-band, a circular corrugated horn, with the model number AF-0800/SL is used. A model, generated by Autodesk Inventor is shown in the appendix A.1. Also the simulated normalized radiation pattern in both reference planes can be found there. The total gain is 15.4 dBi and the nearly rotationally symmetric pattern has a 3 dB beamwidth of 35°. The cross-polar level is better than -42 dB in the X-band.

3.1.2 Simulated Depolarization

The depolarization of the CTR is analyzed for horizontal and vertical polarization. In HFSS this is ensured by rotating the excitation of the corrugated horn by 90°. In each sample point the simulated electric field vector is resolved on a cartesian coordinate system. If the feed is horizontally polarized, the x-component of the field vector forms the co-polarization. Otherwise it is the y-component for vertical polarization. The simulations are evaluated at three different frequencies, 8.2 GHz, 10 GHz and 12.4 GHz, so that the entire X-band is covered.

The cross-polar level describes the ratio between co- and cross-polarization. A quantitative characterization of the cross-polar level of the QZ is performed by introducing two values $\bar{b}$ and $b_{<\text{-}35\,\text{dB}}$. The arithmetic mean of the cross-polar level taken over all samples in the QZ, is expressed in $\bar{b}$. The value $b_{<\text{-}35\,\text{dB}}$ describes the percentage of the QZ's samples, having a cross-polar level better than -35 dB.

For a visual illustration of the cross-polarization level in the QZ, contour plots are used. Fig. 3.2 shows the distribution for the horizontal polarized feed. Along $z = 0$ m, which is the symmetry plane of the CTR, practically no depolarization occurs. It is noted that the minimum cross-polarization is found at $x \approx -0.3$ m, which is not the exact theoretical result. The effect can be explained by taking into account the radiation pattern of the reference feed, shown in appendix A.1. The cross-polar level of the reference feed is not ideal, the imperfections are mapped directly into the field distribution. Along the x-direction the cross-polarization level increases, reaching -22 dB at the upper and lower end of the QZ. This results match with the theoretical considerations. In Fig. 3.2 the spatial cross-polarization level is shown for the vertical polarized reference feed. Again the lowest depolarization is found in along the symmetry plane. The results are similar to the horizontal oriented feed, and therefore not discussed further.

Additional simulation results for the X-band are summarized in Tab. 3.2 and Tab. 3.1. The contour plots visualizing the cross-polarization level for other frequencies are

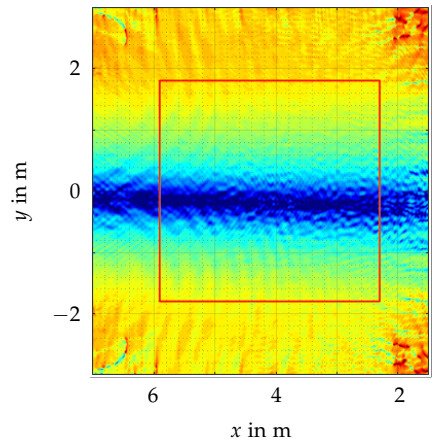

Fig. 3.1: The simulated cross-polar level for horizontal orientation at 10 GHz.

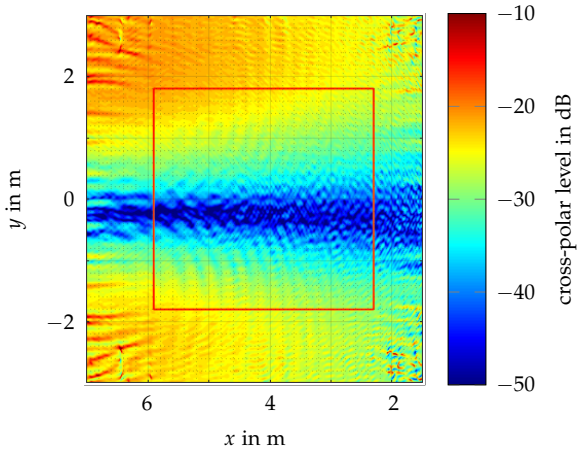

Fig. 3.2: The cross-polar level for vertical orientation at 10 GHz simulated in HFSS.

found in the appendix A.2. Towards lower frequencies the results for vertical and horizontal orientation are very similar. Instead at $f = 12.4\,\text{GHz}$, the shape of the plots changes significantly. The reason for this effect not known, but it is assumed to have its origin in the cross-polarization radiation pattern of the corrugated feed.

Table 3.1: Simulated cross-polar level of the reference horn in h-pol arrangement

	$\bar{b}$	$b_{<\text{-35 dB}}$
8.2 GHz	−33.1 dB	31.7 %
10 GHz	−32.4 dB	28.2 %
12.4 GHz	−31.7 dB	29.2 %

Table 3.2: Simulated cross-polar level of the reference horn in X-band in v-pol

	$\bar{b}$	$b_{<\text{-35 dB}}$
8.2 GHz	−31.8 dB	27.4 %
10 GHz	−32.3 dB	30.0 %
12.4 GHz	−31.2 dB	31.3 %

3.1.3 Measured Depolarization

Additionally to the simulation, the cross-polarization level is also measured. At the DLR this is done by a field probe scanner. The principle is to take electric field samples with a small receiving antenna. In order to have a high spatial resolution of the

sampling points, open waveguide probes are often used. The disadvantage is their poor cross-polar discrimination and low directivity. In the measurements for this work the standard gain horn ANT-SGH-8.2-12.4 from NSI-MI is used. It has a gain of 22.4 dBi, but does not allow a dense sampling due to its larger aperture.

The scanner system of the DLR is shown in Fig. 3.3. It consists of a linear axis having a length of 6.4 m. The scanner is mounted on the roll axis turntable of the positioner, therefore the QZ is scanned circularly. An additional roll axis, rotating the field probe, ensures that it remains polarization matched with the feed antenna. This setup has its technical limitations: For example the finite stiffness of the linear axis makes accurate phase measurements in the X-band impossible. For this work it is no restriction, since only the amplitude is relevant. As seen in Fig. 3.3, the linear axis can not be covered with absorbing material and therefore it causes strong reflections and diffractions. This effects degenerate the quality of the obtained measurements [31].

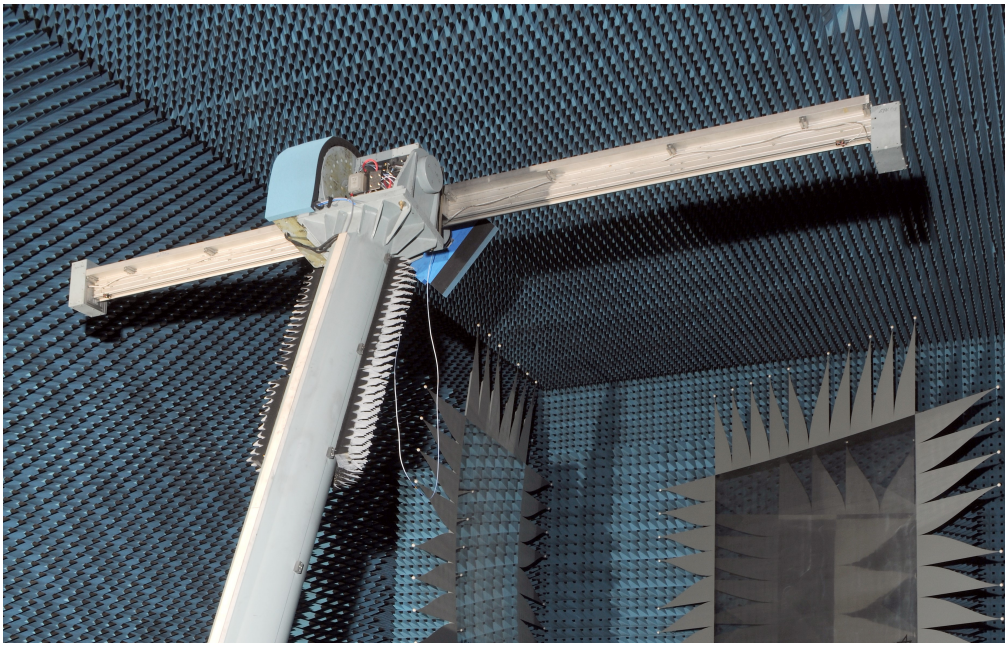

Fig. 3.3: The used scan axis.

The h-pol results in Fig. 3.4 are measured on the xy-plane at $z = -9.5\,\mathrm{m}$, which is the same as for the simulations. Due to the scanner, the plot has a circular shape with a radius of 2.25 m. Different restrictions in the measurement setup, do not allow a larger scanning radius. Both plots the simulation in Fig. 3.1 and the scanning in Fig. 3.4 show similar results, which is validating the simulation setup in HFSS. The cross-polar level increases towards the upper and lower edge of the QZ to $-27\,\mathrm{dB}$.

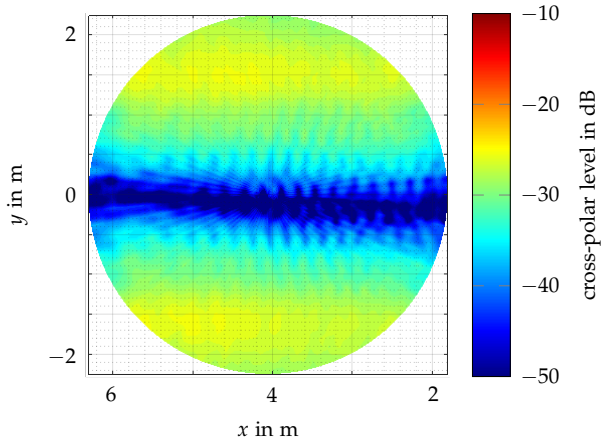

Fig. 3.4: The measured cross-polar level of the reference feed in h-pol configuration. The frequency is 10 GHz.

3.2 Development of the Feed

The development of the feed is divided in several parts. Different techniques are presented, which can compensate the increased cross-polarization level. One of them, the conjugate matched field concept, is used to design an improved feed structure. In a first step, together with the DLR, the following requirements are made:

- The operating frequency band is in the X-band, from 8.2 GHz to 12.4 GHz. So the complete bandwidth of a standard WR90 rectangular waveguide can be used.
- The concept must be generating a linear polarized field, horizontal and vertical.
- Compatible with the feed positioning system of the CTR. This limits the maximum size and weight of the new feed.
- Providing a significant lower cross-polar level in the entire QZ, while not weaken the co-polarized fields.
- The co-polarized fields in the QZ must have a maximum deviation in amplitude of 1 dB peak to peak. The variation in phase must be less than $\pm$ 5°.
- The size of the QZ of approximately 3.6 m in width and height should be preserved.

3.2.1 Compensation Techniques

There exist different methods for compensating the depolarization effect in a CATR. One is the principle of the compensated CATR, presented in Section 2.3. This is not

practical since it would require new reflectors and significant interventions in the chambers structure. The costs of such a redesign are too high.

Postprocessing

The key principle behind this methods is to use knowledge of the imperfect field distribution in the QZ, for a calibration of the measurements. An advantage is that the co-and the cross-polar performance can be improved simultaneously. The correction data can be gathered by direct measurements of the fields in the QZ, or by using simulations. Both methods are presented in [31].

The method of field probe scanning, is presented in detail in Section 3.1.3. The postprocessing correction uses the obtained measurements of amplitude and phase. A second method is to use a RCS target. The RCS of a flat plate is known, and it is rotated in the QZ. The received signal is processed by a far field to near field transformation, and the corresponding field distribution in amplitude and phase is calculated. It is used similar as the field probe measured data. A drawback is that the RCS measurement requires two antennas in the feed position. The calibration set up is therefore not directly applicable for other feed antennas. Often this technique is used in correcting RCS measurements.

It is also shown that Physical Optics (PO) simulation results are also valid for corrections. The improvement is strongly dependent, how accurate the feed antenna is remodeled in the simulation. In [31] also a hybrid correction is suggested, combining PO simulated data and direct measurements.

Conjugate Matched Field Concept

The conjugate matched field concept is directly related to the phenomenon of destructive interference. The combination of two harmonic waves $m_1(t) = m\sin(\omega t + \phi_1)$ and $m_2(t) = m\sin(\omega t + \phi_2)$, with equal amplitude m but different phases, is

$$m_{\text{comb}}(t) = m\sin(\omega t + \phi_1) + m\sin(\omega t + \phi_2) = 2m\cos\left(\frac{\phi_1 - \phi_2}{2}\right)\sin\left(\omega t + \frac{\phi_1 + \phi_2}{2}\right). \tag{3.1}$$

In (3.1) the trigonometric addition theorem is used [29, p. 124]. The sin-term describes the oscillation of the combined wave, while the expression involving the cosine, affects the amplitude. If the phase difference is $\phi_1 - \phi_2 = \pi$ the cos-expression is 0 and both waves are canceled (destructive interference). Otherwise for $\phi_1 - \phi_2 = 0$ the amplitude gets doubled (constructive interference). In case of transverse waves, like electromagnetic waves are, it is evident that the polarization states of both $m_1(t)$ and $m_2(t)$ must coincide. Based on this consideration the cross-polarization generated by the offset geometry can be suppressed by a destructive interference with an adequately polarized wave, the so called conjugate matched field.

In [7] polarization grids are placed in front of the feed, to affect the polarization. These grids consist of periodicly arranged, separated metal strips. In [7] the grids are optimized for a single reflector CTR but the principle is not limited to this case. The grid manipulates the radiated field, to cancel the cross-polarization. A full wave verification of the concept applied to a reflector antenna is found in [32]. A drawback is, that for the horizontal and vertical polarization state, different grids has to be used.

As an alternative, lens horn antennas are suggested in [33], where the shape of the dielectric lens is chosen to generate the conjugate matched field. By this method also a desired tapering of the electric field, illuminating the reflector, can be generated. In [33] the antenna is analyzed simulatively and improves the cross-polar level. The drawbacks of this concept are the dielectric losses causing a reduced gain and a limited bandwidth.

The conjugate matched field can be generated directly by the feed. In [8] a tri-mode horn is suggested for single reflector systems. Additionally to the fundamental TE_{11} mode, the horn supports the propagation of a TE_{21} mode. This generates a field distribution, matching the desired conjugate field pattern. In order to form an axially symmetric radiation pattern a TM_{11} mode is used. The two non fundamental modes are excited by discontinuities inside the horn. In [8] the concept is validated by PO simulation results, showing a cross-polar level of better than $-35\,\mathrm{dB}$. The concept although suffers from a limited bandwidth, which is 250 MHz in the X-band. There exist different techniques to improve the bandwidth but not enough to fulfill the requirements. Additionally this design is difficult to adapt for a use in both horizontal and vertical polarization.

Instead of using higher order modes for compensation, a feed array can be developed, having the advantage of a high design flexibility. In principle it is the same as for the tri-mode horn, but the co-polarized field and the conjugate matched field are generated by different radiating elements. In [9] a feed array is designed and validated in an single reflector CATR. The array consists of three elements, where the central element, a choke ring antenna generates the co-polarized field. The outer antennas excite the orthogonal polarized, conjugate matched field. In simulations the concept is verified in a frequency range from 10 GHz to 15 GHz, improving the cross-polar level down to $-40\,\mathrm{dB}$. The large bandwidth and the high flexibility in design, are the reasons why new feed is based on the findings published in [9].

3.2.2 Feed Horn

For consistent nomenclature the new feed is called "feed array", while the currently used corrugated horn, is called "reference feed". The element of the feed array generating the co-polarized field is named "co-horn", and the conjugate matched field is created by two "cross-horns".

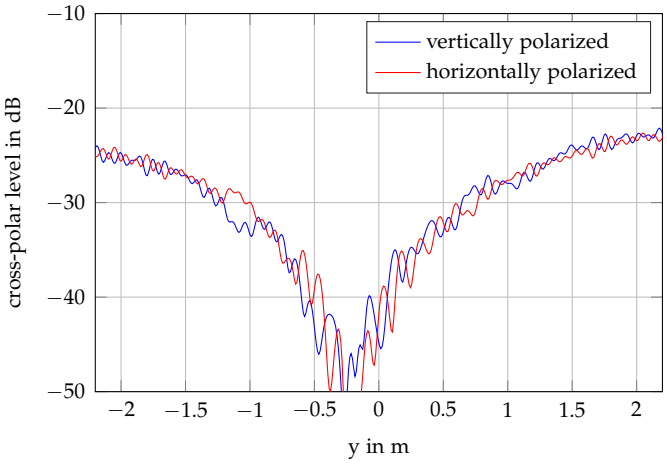

Fig. 3.5: The simulated cross-polarization of the chamber along a cut at x = 4.1 m.

Cross-Horns

The conjugate matched field concept requires a detailed analysis of the depolarization caused by the offset geometry. This is done in HFSS simulations in Section 3.1.2 and in Section 3.1.3 on the basis of measurements. Both show that the cross-polarization level is predominantly increasing along the y-direction. In the symmetric plane of the CTR at $y = 0\,\text{m}$, practically no depolarization occurs, but at $y = \pm 1.9\,\text{m}$ (the upper and lower end of both reflectors) the cross-polarization has the highest values. Additionally the cross-polarization is symmetric to the plane at $y = 0\,\text{m}$. This holds true for both vertical and horizontal main polarization, meaning the same feed array geometry can be used for both cases. The slight depolarization along $-x$-direction is ignored, because a cancellation leads to a disproportional increase in complexity.

Fig. 3.5 shows an one dimensional plot of the cross-polar level simulated in HFSS at 10 GHz. Both graphs are plotted along the y-axis in the center of the QZ, at $x = 4.1\,\text{m}$ for both polarization states. This representation gives a deeper insight than the contour plots. All parts outside the range $y = \pm 1.9\,\text{m}$ (outside the reflector's projection) are not considered, they are generated by diffraction processes. In Fig. 3.5 the minimum cross-polar level has an offset of $-25\,\text{cm}$ related to the symmetry plane. This is explained by the non perfect, non cross-polarization free radiation pattern of the reference feed (see A.1). A more detailed analysis is not performed. In agreement with the theory of depolarization in offset reflectors, the minimal cross-polarization is assumed to be at $y = 0\,\text{m}$.

The resulting distribution looks similar to a difference field monopulse pattern, like in [10, p. 772]. An array radiation pattern is a combination of the single element pattern, C_{el}, and the array factor, C_{af}, which describes the geometry and location of the array. Therefore it is convenient, to synthesize first an adequate array factor, having a

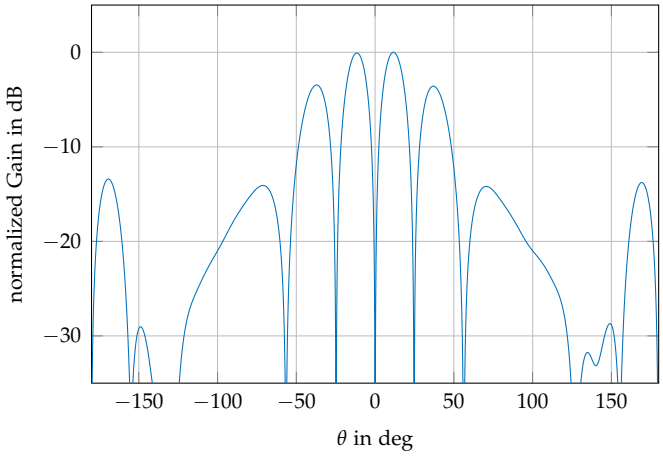

Fig. 3.6: The difference field monopulse pattern of the cross-horn array, including the grating lobes.

monopulse characteristic. In [13, pp. 89] a two element array, fed with equal amplitude and a phase difference of $\delta_P = 180°$, has the normalized array factor of

$$C_{\text{af}} = \sin\left(\beta \frac{d}{2}\cos(\theta)\right), \qquad \text{with} \quad \beta = \frac{2\pi}{\lambda}. \tag{3.2}$$

The phase constant is denoted by β and θ describes the angular variation in far field while the distance between the elements is described by d. Like seen in (3.2) the ratio d/λ has a significant influence on the array factor. Additionally, if the distance exceeds λ, the problem of grating lobes arise.

In a first step the radiation pattern is synthesized, in order to ensure both monopulse peaks illuminate the upper and lower edge of the sub-reflector. The angular distance between both peaks is denoted by γ_{mono} and directly related to the distance to the sub-reflector. Considering the geometric relation γ_{mono} must be 23°. Based on (3.2) this results in $d = 72\,\text{mm}$, causing grating lobes, which require proper treatment.

As elements, open cylindrical waveguides are used. They support horizontal and vertical polarization, without need to be rotated. They are standardized components and can be bought in high quality. The normalized opening diameter of X-band components is 23.83 mm and the length of the antenna is 110 mm, a drawing containing all dimensions is found in the appendix A.5. A model of the cross-horn subarray is analyzed in HFSS, the simulated radiation pattern is shown in Fig. 3.6, where the effect of the grating lobes are visible. Since they do not illuminate the sub-reflector, it is not a problem.

Co-Horn

Section 2.3 explains how a CTR generates a nearly plane wave in the QZ, including the imperfections of the field distribution from an ideal plane wave. The tapering in

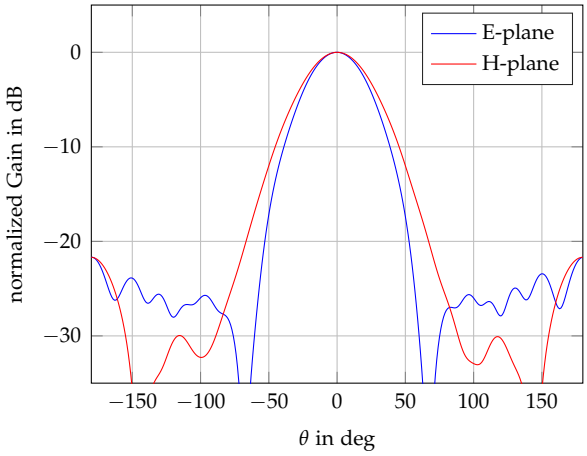

Fig. 3.7: The simulated radiation pattern of the co-horn in two orthogonal cuts.

the amplitude is directly related to the co-polarized radiation pattern of the feed. In order to minimize the tapering, the sub-reflector should be illuminated uniformly. This is typically realized by a low gain feed with a large 3 dB beamwidth. On the other hand the serrated edges should be illuminated minimal, otherwise strong diffractions cause an increase in the phase and amplitude ripples. In dual reflector systems a broad radiation pattern causes an additional error source, namely a direct illumination of the main reflector causing triple reflections. Furthermore, since the cross-horn array only compensates the cross-polarization caused by the offset geometry, the co-horn must have a very low cross-polarization.

In order to support horizontal as well as vertical polarization, a conical horn design is chosen. A major constraint is the limited size, because it has to be placed between the cross-horns. The horn is designed and optimized in HFSS, and the final dimensions are shown in the technical drawing in appendix A.5. Horn antennas with corrugations provide higher cross-polarization purity and a rotationally symmetric radiation pattern. This is not possible because adding corrugations with a depth of $\lambda/4$ would exceed the size restrictions.

In Fig. 3.7 the normalized radiation pattern in two orthogonal cuts for 10 GHz is shown. The total gain is 12.6 dBi, the 3 dB beamwidth is 42° in E-plane and 48° in H-plane. In the X-band the reflection coefficient (S_{11}) is below -20 dB. The part of the pattern illuminating the sub-reflector has a cross-polar level of better than -45 dB, holding true for the X-band.

Feed Array

The generation of a plane phase front requires that the phase center of the co-horn is placed in the focal point of the CTR. For a optimum compensation of the cross-polarization level, the same holds true for the phase center of the subarray formed by

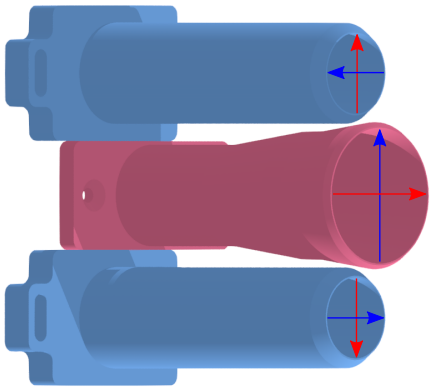

Fig. 3.8: A schematic illustration of the polarization direction, blue is vertically and red is horizontally polarized.

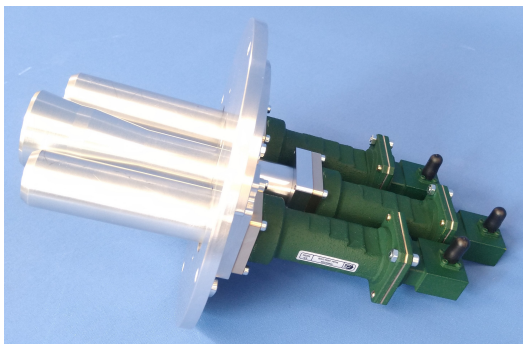

Fig. 3.9: The manufactured feed array.

the cross-horns. In order to fulfill both requirements the elements are combined to form a linear, equally spaced array. The spacing distance is denoted by $d/2$, see the drawing in the appendix A.5, and subject to optimization. The previously calculated value $d = 72\,\text{mm}$ is based on a geometrical examination of the CTR but not on direct simulation results. It is simulatively found that a distance of 84 mm provides higher cross-polar level in the X-band. This deviation is explained by the dense assembly of the individual parts, influencing the radiation pattern.

For manufacturing, the design is remodeled in Autodesk Inventor, like shown in Fig. 3.8. Some adaptions, considering the manufacturing technique are made, like the wall thickness of 3 mm and the design of a mounting plate. In Fig. 3.9 the final assembly is visible, the three horns together with the cylindrical mounting plate are manufactured in the institute's mechanical laboratory. The other parts are standardized waveguide components from Flann Microwave Ltd.

All feed antennas at the DLR have an impedance wall, which minimizes the direct illumination of the main-reflector and reduces the problem of triple reflections. For the feed array a similar impedance wall is designed but due to the larger dimensions of the feed array, the impedance wall is also larger. The currently used mounting plate is too small to support the new designed impedance wall. It would require several adjustments, which is very time consuming. In the course of this thesis the feed array is used without it. It is evident that this will cause higher disturbances in the measured field distribution, but it will be discussed in more detail in Section 4.2.

All three horns must be excited with the correct polarization direction, to provide the desired performance. In Fig. 3.8 the polarization states of the elements are indicated by colored arrows in the aperture. The polarization state of the co-horn indicates, if the QZs field is horizontal (blue colored arrows) or vertical (red coloredarrows) orientated. To fulfill the conjugate matched field principle, both cross-horns are orthogonal polarized.

Like previously stated the orientation of the feed array remains the same for both polarization states, only the directions of the excitation are changed. The necessary phase shift of 180° between both cross-horns, to generate the monopulse radiation characteristic, is ensured frequency independent by opposed polarization directions, visualized in Fig. 3.8.

3.2.3 Feed Network

The feeding network ensures the correct excitation, in amplitude and phase of the individual array elements. The proof of concept demonstrator is simplified, and consists only of lumped elements. In Fig. 3.10 the schematic of the network is shown, it is made up of a line coupler, two phase shifters, an attenuator and a Wilkinson divider.

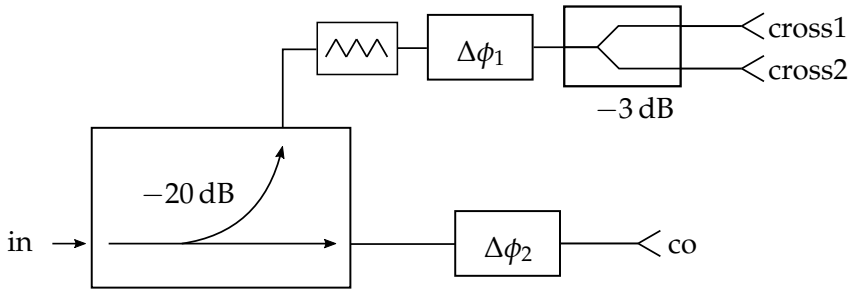

Fig. 3.10: Schematic of the feeding network.

The simplified design has some limitations in adjusting the excitation factors. Conditioned by the Wilkinson divider the amplitude of both cross-horns is the same. The outputs of an ideal Wilkinson divider have a phase difference of 0°. Like previously stated, the polarization states of the cross-horns are opposed, enforcing a 180° phase shift, independent of the frequency. In the X-band the attenuator has a uniform attenuation over the frequency, therefore the amplitude ratio between the co-horn and cross-horns has a frequency independent, constant value. Since a phase shifter is a true delay line, its phase relation changes linearly over frequency, other waveforms are not possible.

3.2.4 Numerical Optimization

The radiation pattern of an antenna array can be modified by the amplitude and phase relation, by which the individual elements are excited. They are called weighting factors. Array synthesis describes the process of their determination to realize a desired pattern. In [34] an array synthesis is shown based on a numeric, convex optimization. The generalized problem formulation is,

$$C(\theta, \phi) = \boldsymbol{w}^{\mathrm{T}} \boldsymbol{s}(\theta, \phi)\,. \tag{3.3}$$

The vector $\boldsymbol{w}$ contains the complex valued weighting factors, and the individual far field properties of the elements is in the vector $\boldsymbol{s}(\theta, \phi)$. The formulation in 3.3 can also be extended to include coupling or other effects, the array pattern remains a linear function of the weighting factors [34].

The determination of the optimized weightings of the feed array is divided in two parts. First, in order to reduce the complexity, the optimization is performed at a single frequency. The calculation of the weightings, optimized for the entire X-band is done in a second step. For the broadband optimization the limitations of the feeding network in Section 3.2.3 must be considered.

Single Frequency Optimization

In the context of this work the near field distribution is relevant. Therefore the problem formulation from (3.3) must be adapted. The goal is to minimize the cross-polar level in the QZ on a plane at $z = -9.5\,\mathrm{m}$, by adapting the weighting coefficients. A simulation in HFSS calculates the distribution of the cross-polar level in the QZ of each element. The distributions are summarized in the vector

$$\boldsymbol{s}(x, y) = \left[s_{\mathrm{co}}(x, y), s_{\mathrm{cross1}}(x, y), s_{\mathrm{cross2}}(x, y)\right]^{\mathrm{T}} .$$

The different field distributions are indicated by the indices. Since each near field sample consists of complex numbers, $\mathbf{s}(x, y)$ is also complex valued. In

$$\boldsymbol{w} = \left[w_{\mathrm{co}}, w_{\mathrm{cross1}}, w_{\mathrm{cross2}}\right]^{\mathrm{T}}$$

the individual weighting factors are summarized, leading to the complex valued vector $\mathbf{w}$. Based on the definition the problem statement for the optimization can be written like

$$\begin{aligned} \min_{\boldsymbol{w}} \quad & \mathrm{mean}\left\{\left|\boldsymbol{w}^{\mathrm{T}}\boldsymbol{s}(x, y)\right|\right\} \\ \text{s.t.} \quad & |w_{\mathrm{co}}| = 1\,, \\ & |w_{\mathrm{cross1}}| = |w_{\mathrm{cross2}}|\,, \\ & \mathrm{phase}(w_{\mathrm{cross1}}) = 0\,. \end{aligned} \tag{3.4}$$

In order to minimize the cross-polarization over the entire QZ, the arithmetic mean in taken over the resulting distribution. The side constrains ensure a normalization of the co-horn's amplitude, additionally both cross-horns are excited by the same amplitude. The 360° ambiguity of the phase allows to arbitrarily set the phase of one weighting coefficient. In this case $\mathrm{phase}(w_{\mathrm{cross1}})$ is fixed to 0°. This yields to an optimization problem with three variables. Since the individual near field distributions are combined by the superposition principle, no coupling effects are regarded in the optimization. In simulations the coupling is low enough, to justify this simplification.

Table 3.3: Initial values for the numerical optimization

	w_{co}	w_{cross1}	w_{cross2}
$\lvert w\rvert$	1 W	1 mW	1 mW
phase(w)	0°	0°	180°

Table 3.4: Optimized weighting factors at 10 GHz for v-pol

	w_{co}	w_{cross1}	w_{cross2}
$\lvert w\rvert$	1 W	0.93 mW	0.93 mW
phase(w)	−87.5°	0°	178.1°

The optimization itself is carried out in MATLAB by the nonlinear programming solver "fmincon". It finds the local minimum of a nonlinear, multi variable and constrained function. For the solving algorithm, different procedures, presented in 2.4, can be used. Fmincon does not allow an optimization with complex variables. A workaround is found by separating vector $\boldsymbol{w}$ into amplitude and phase, the same is done for the side constraints [35]. The actual optimization is carried out by the interior points principle. The dedicated method in fmincon uses different improvements to further increase the performance. For example there exist two main types of steps in each iteration. This allows to treat locally non convex problems properly. Additionally MATLAB allows adaptions in several steps of the interior point algorithm, to further increase the performance. In [36] a comprehensive discussion is found.

The optimization problem in (3.4) is not necessarily convex. Depending on the distribution, it is possible to have multiple local optimums. Finding the global optimum under these conditions requires a well chosen starting point for the first iteration. It is determined by analyzing the simulated and the measured cross-polarization distribution in Section 3.1.2 and Section 3.1.3. The initial values are summarized in Tab. 3.3. The 180° phase shift between phase(w_{cross1}) and phase(w_{cross2}), is evident, since it is necessary to form the monopulse radiation characteristic. Given the fact, that the cross-polar level is approximately −30 dB at the upper and lower edges of the QZ, the initial value of $\lvert w_{\text{cross1}}\rvert$ and $\lvert w_{\text{cross2}}\rvert$ is set to 1 mW (−30 dBm).

It is evident that the described optimization is only valid for a single frequency, namely the frequency at which the near fields are calculated. In Tab. 3.4 and Tab. 3.5 they are shown exemplary for 10 GHz. Additionally the weighting factors depend on if the feed is used for generating a vertical or horizontal polarized field. A summary of the optimized weighting factors is found in the appendix A.4.

Table 3.5: Optimized h-pol weighting factors at 10 GHz

	w_{co}	w_{cross1}	w_{cross2}
$\lvert w \rvert$	1 W	1.21 mW	1.21 mW
phase(w)	94.8°	0°	178.2°

X-band Optimization

The optimization algorithm for the X-band is divided in several parts. The problem is to approximate the frequency dependent, optimum weightings without violating the limitations of the feeding network. Evidently, the limited capabilities of the network, reduce the cross-polarization compensation performance.

One constraint of the feeding structure is the 180° phase shift between both cross-horns. Mathematically speaking this means that the side constraints in (3.4) must be adapted. The updated optimization problem is

$$\begin{aligned} \min_{\boldsymbol{w}} \quad & \text{mean}\left\{\left|\boldsymbol{w}^{\mathrm{T}}\boldsymbol{s}(x,y)\right|\right\} \\ \text{s.t.} \quad & |w_{\text{co}}| = 1\,, \\ & w_{\text{cross1}} = -w_{\text{cross2}}\,, \\ & \text{phase}(w_{\text{cross1}}) = 0\,. \end{aligned} \tag{3.5}$$

This reduces the problem complexity to two variables: $|w_{\text{cross1}}|$ (resp. $|w_{\text{cross2}}|$) and phase(w_{co}).

As seen in the appendix A.4 the optimum excitation vector changes over frequency. A deeper understanding is found by solving (3.5) for five frequency points in the X-band, namely 8.2 GHz, 9 GHz, 10 GHz, 11 GHz and 12.4 GHz. The results for h-pol configuration are plotted as blue colored dotes in Fig. 3.11 and Fig. 3.12. In Fig. 3.11 it can be seen that for increasing frequency the amplitude of w_{cross1}, is decreasing, especially visible at 12.4 GHz. The attenuator in the feeding network is constant over frequency, therefore the optimum values can not be matched. The best trade off is to take the average over all sample points, leading in h-pol configuration to $|w_{\text{cross1}}|$ = 1.164 mW.

Since the phase shifters in the feeding network are true delay line devices, the phase relation varies linearly over frequency. As seen in Fig. 3.12 the optimized values for phase(w_{co}) are decreasing. A linear regression curve is calculated based on the sample points by the linear least squares method. The red colored dashed line in Fig. 3.12 visualizes that, exemplary for the h-polarization configuration. The slope is -44.9 deg/GHz.

In a last step the hardware realization of the feeding network has its limitations, starting with the amplitude of the cross-horns. The prototype of the network, uses fixed attenuators. Even a combination of several components does not allow to realize

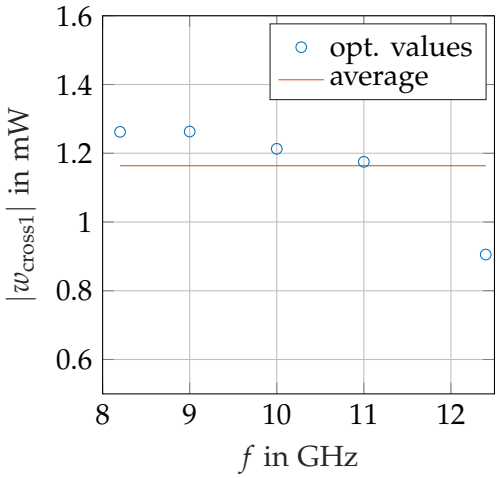

Fig. 3.11: The optimized values for $|w_{\text{cross1}}|$ in h-pol configuration. The red line shows the frequency constant average.

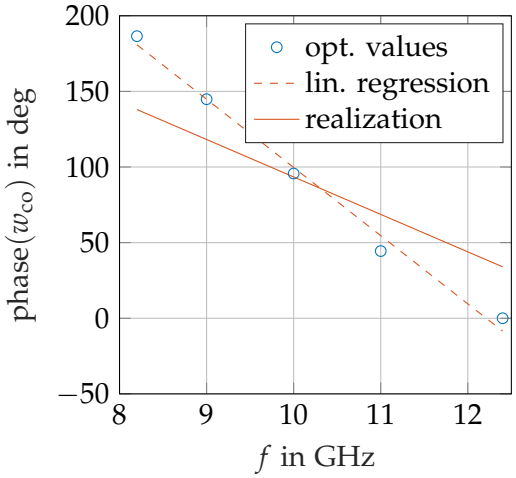

Fig. 3.12: For h-pol configuration the optimized phase values, including the linear regression curve.

the desired attenuation, since the step size is limited. In the present case the smallest available attenuation is 0.25 dB. The best possible realization for the h-polarized configuration is $|w_{\text{cross1}}| = 1.23\,\text{mW}$, giving a deviation of 5.6 % from the ideal value.

For the phase relation of phase(w_{co}) similar limitations apply. The setup of the network in Fig. 3.10 does not allow to realize the optimized linear regression curve. With the used phase shifters it is only possible to realize the slope of the curve or a desired point, not both. The network is adapted to have the best compensation performance around 10 GHz, resulting in a slope of $-24.7\,\text{deg/GHz}$. It is visualized by the red colored continuous line in Fig. 3.12.

4 Simulative and Measurement Results (h-pol)

In this section the concept is validated by HFSS simulations and measurements in the CTR. In order to short the discussion only the horizontal feed array configuration is considered.

4.1 Simulative Results

In Section 3.2.2 the development of the feed array is presented extensively. Important design parameters, which are used in the simulative validation, are summarized in the following: The distance between both cross-horns is 82 mm. The limitations of the feeding network are considered by using the realized weighting factors $|w_{\text{cross1}}| = 1.23\,\text{mW}$ and the slope of $\text{phase}(w_{\text{co}}) = -24.7\,\text{deg/GHz}$.

The simulation environment for the feed array is the same as for the currently used reference feed antenna. It is summarized in Section 3.1.1. Due to the higher complexity and three individual excitations the computational time increases to 109 h.

4.1.1 Co-Polarized Field

The feed array must preserve the co-polar performance of the CTR, therefore a comparison between the reference feed and the feed array is made. Since the requirements for the amplitude uniformity are more strict, than for the phase, the co-polar amplitude is analyzed exclusively. In Fig. 4.1 the normalized co-polarization level is shown in the QZ at a frequency of 10 GHz. The projection of the main-reflector is marked by a red colored rectangle. Several errors, explained in Section 2.3.2, are visible in Fig. 4.1. The irregular fluctuations in the amplitude are caused by diffraction processes. Additionally, the field tapering is noticeable, explaining the decreasing amplitude in $-x$-direction.

The same errors are present in Fig. 4.1. It shows the normalized co-polarization level of the CTR fed by the feed array at a frequency of 10 GHz. Due to the larger 3 dB beamwidth, it can be seen that the field tapering is minimized, compared to Fig. 4.1.

In order to quantify and compare the co-polar performance, a parameter σ_{co} is defined. It describes the sample standard deviation, a measure for the variation of the samples, referred to the mean value. In table 4.1 the sample standard deviation is calculated for the X-band, showing that the co-polar performance of the feed array is comparable to the reference feed.

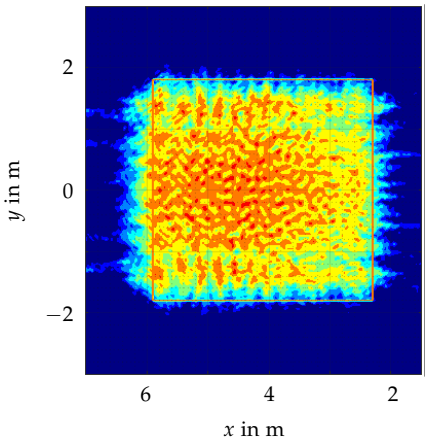

Fig. 4.1: The normalized reference co-polarization level for horizontal orientation at 10 GHz, simulated in HFSS.

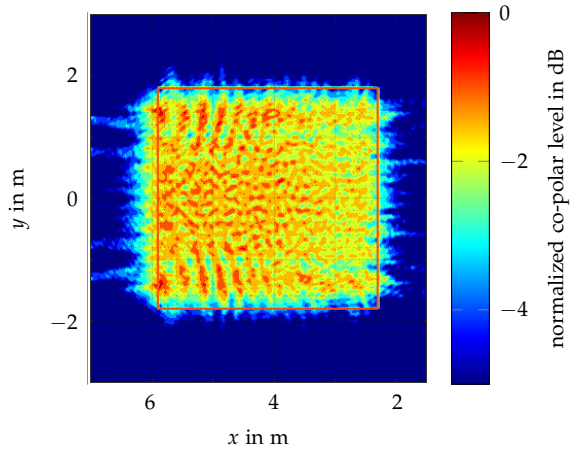

Fig. 4.2: The normalized co-polarization level of the QZ field generated by the feed array at 10 GHz.

Table 4.1: A quantitative comparison of the co-polarization performance, over the X-band

	reference feed	feed array
8.2 GHz	0.658	0.686
10 GHz	0.694	0.620
12.4 GHz	0.866	0.632

4.1.2 Cross-Polarized Field

In Fig. 4.3 the simulated cross-polar level of the feed array in the QZ is shown. The simulation is performed at 10 GHz for h-pol configuration. Compared with the plot of the reference feed in Fig. 3.1, the improvement is evident. Especially the depolarization effect, causing an elevated cross-polarization towards the upper and lower edge of the main-reflector, is compensated. At 10 GHz the mean cross-polar level is −40.8 dB compared to −32.4 dB of the reference feed. In the appendix A.3 the simulation results for 8.2 GHz and 12.4 GHz are shown.

A summary of the results in the X-band can be found in Tab. 4.2 and Tab. 4.3. The definition of the values $\bar{b}$ and $b_{<\text{-}35\,\text{dB}}$, is the same as in Section 3.1.2. Around 10 GHz the cross-polarization is effectively suppressed. Towards the ends of the X-band the performance degenerates, since the ideal phase for w_{co} can not be achieved by the network.

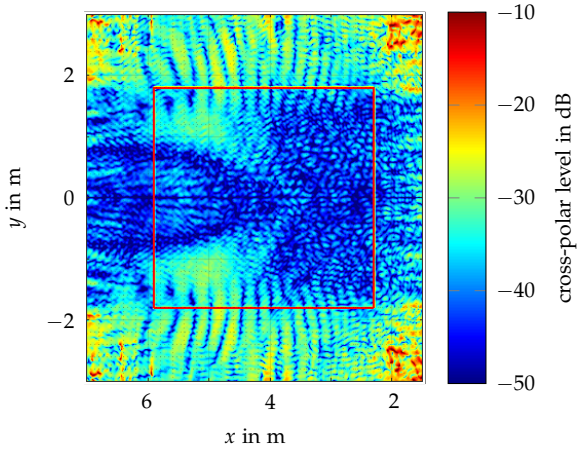

Fig. 4.3: The simulated cross-polar level of the QZ field generated by the feed array at 10 GHz.

Table 4.2: Comparison of the mean cross-polar level ($\bar{b}$) between reference feed and feed array

	reference feed	feed array
8.2 GHz	−33.1 dB	−33.2 dB
9 GHz	−32.5 dB	−36.8 dB
10 GHz	−32.4 dB	−40.8 dB
11 GHz	−32.2 dB	−37.2 dB
12.4 GHz	−31.7 dB	−31.5 dB

Table 4.3: Comparison of the $b_{<\text{-}35\,\text{dB}}$ value between reference feed and feed array

	reference feed	feed array
8.2 GHz	31.7 %	33.5 %
9 GHz	28.6 %	57.4 %
10 GHz	28.2 %	80.9 %
11 GHz	27.7 %	56.0 %
12.4 GHz	29.2 %	22.7 %

4.2 Measured Results

The measurement of the field distribution generated by the feed array is obtained by the field probe scanner. In Section 3.1.3 the measurement setup is explained in detail for the reference feed, it does not change for the feed array. The design parameters for the feed array are the same as for the simulative validation: A distance of 82 mm between the two cross-horns and using the realized weighting factors. In the following only the results for the horizontal polarization configuration are presented.

Like mentioned the feed array is not equipped with an impedance wall, like usually a feed antennas would be. This causes higher field disturbances due to the direct illumination of the main-reflector and the occurring triple reflections. A way to compare the feed array with the reference feed, which is measured with an impedance wall, is to use a different time-gating. The length of the time-gating can be adjusted arbitrarily, in measurements it is usually 250 cm. For the reference feed this value is used, since it suppresses the direct illumination.

For the feed array two different time-gate lengths are used 250 cm and 150 cm. The short value suppresses additionally the triple reflection path. In a measurement of an AUT such a short time-gate would usually not be possible, since the dimensions of the AUT must always be shorter than the time-gate length. It is justified in this case to visualize the influence of the triple reflections and to have comparable results.

4.2.1 Co-Polarized Field

The cross-polar level in Fig. 4.4 is obtained by the reference feed at a frequency of 10 GHz in h-pol configuration and with a time-gate of 250 cm. Fig. 4.5 shows the measurement results at the same frequency but with the feed array and an equal time-gate. In Fig. 4.6 the time-gating is reduced to 150 cm, this also reduces the ripples in the QZ. A more quantitative analysis is found in Tab. 4.4, where the sample standard deviation is shown for different frequencies.

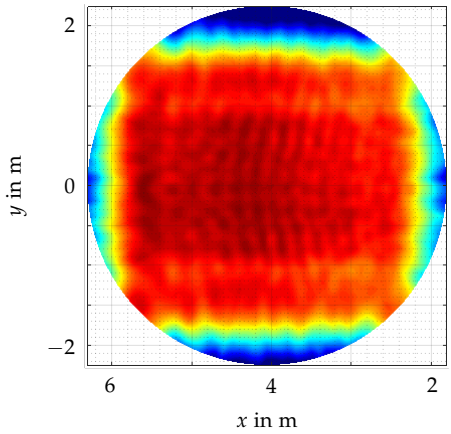

Fig. 4.4: Normalized co-polar level of the QZ field generated by the reference feed at 10 GHz. The time-gate has a length of 250 cm.

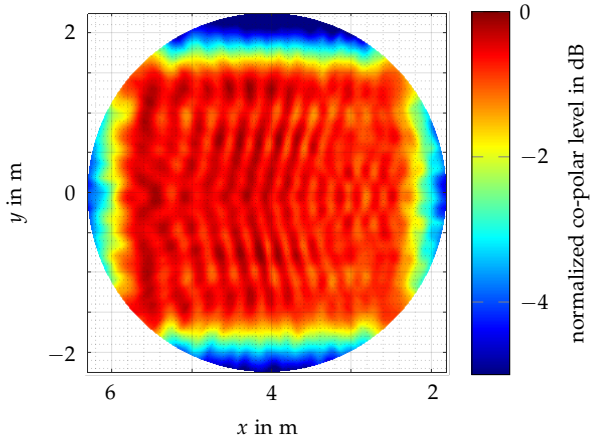

Fig. 4.5: Normalized co-polar level of the QZ field generated by the feed array at 10 GHz. The time-gate has a length of 250 cm.

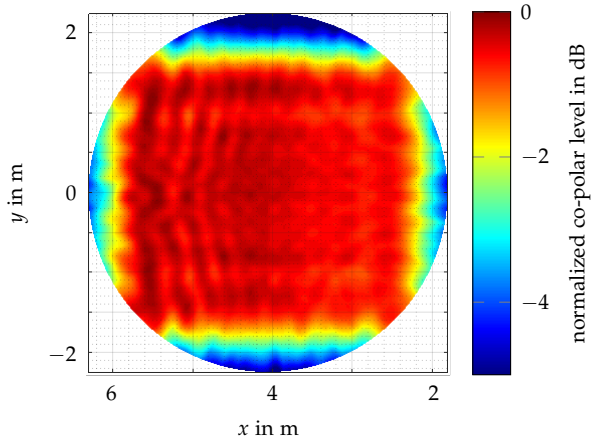

Fig. 4.6: Normalized co-polar level of the QZ field generated by the feed array at 10 GHz. The time-gate has a length of 150 cm.

Table 4.4: A quantitative comparison of the co-polarization performance between reference feed and feed array, measured by the σ_{co} value

	reference feed	feed array (250 cm)	feed array (150 cm)
8.2 GHz	0.478	0.562	0.480
10 GHz	0.549	0.480	0.464
12.4 GHz	0.637	0.513	0.512

4.2.2 Cross-Polarized Field

In Fig. 4.7 the cross-polar level is measured at 10 GHz, for the feed array with a time-gate of 250 cm. The not suppressed triple reflections causing the visible diffractions. The same configuration with the short time-gate (150 cm) is shown in Fig. 4.8. Compared with the reference horn in Fig. 3.4 the depolarization along the y-axis is successfully suppressed. The results for the entire X-band are summarized in Tab. 4.5 and Tab. 4.6. Especially at 10 GHz the mean cross-polar level is suppressed to -41.6 %, a improvement of over 9 dB compared with the reference. At the upper and lower end of the X-band the mean cross-polar level is higher than for the reference feed. This can be explained by the non ideal feeding network. The optimum value for phase(w_{co}) can not be achieved, and the destructive interference does not occur. In fact this leads to an overcompensation, which causes the elevated mean cross-polar level.

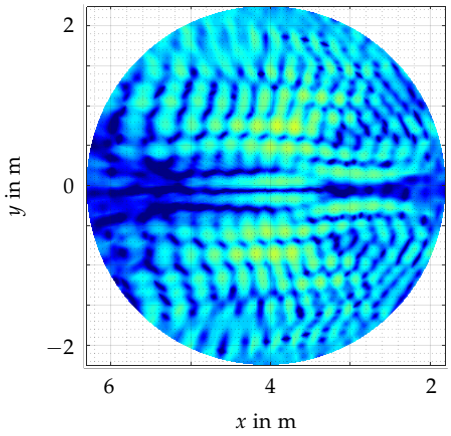

Fig. 4.7: Measured cross-polar level of the QZ field generated by the feed array at 10 GHz. The time-gate has a length of 250 cm.

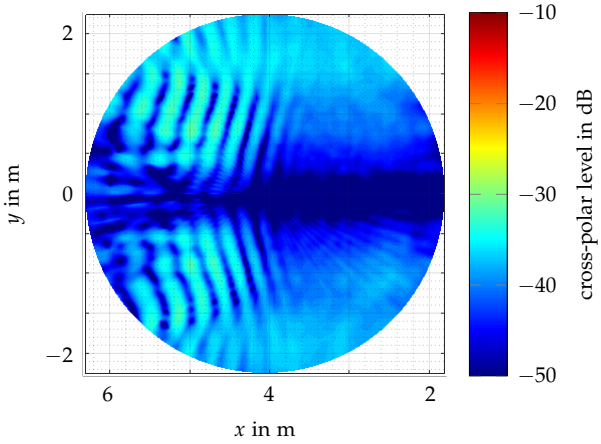

Fig. 4.8: Cross-polar level of the QZ field generated by the feed array at 10 GHz. The time-gate has a length of 150 cm.

Table 4.5: The mean cross-polar level ($\bar{b}$) of the h-pol measurement over frequency

	reference feed	feed array (250 cm)	feed array (150 cm)
8.2 GHz	−32.7 dB	−27.3 dB	−28.1 dB
9 GHz	−33.5 dB	−28.6 dB	−30.0 dB
10 GHz	−32.5 dB	−38.0 dB	−41.6 dB
11 GHz	−33.0 dB	−31.7 dB	−32.2 dB
12.4 GHz	−33.1 dB	−26.7 dB	−26.7 dB

Table 4.6: The $b_{<\text{-}35\,\text{dB}}$ value of the h-pol measurement over frequency

	reference feed	feed array (250 cm)	feed array (150 cm)
8.2 GHz	29.6 %	10.9 %	15.5 %
9 GHz	32.1 %	13.8 %	19.8 %
10 GHz	27.2 %	68.2 %	91.9 %
11 GHz	29.4 %	24.9 %	25.9 %
12.4 GHz	29.7 %	12.0 %	12.0 %

Additionally to Tab. 4.5 and Tab. 4.6 the measured X-band behavior is visualized in Fig. 4.9, Fig. 4.10 and Fig. 4.11. On the x-axis the frequency is shown, while on the y-axis a vertical cut through the middle of the QZ is plotted. The reference feed in Fig. 4.9 has a nearly constant cross-polar performance over the frequency. In Fig. 4.10 the cross-polar level of the feed array with the long time-gate of 250 cm is visualized. In a range from 9.8 GHz to 10.7 GHz the depolarization is compensated. A similar behavior can be seen in Fig. 4.11, but without the artifacts, since the triple reflection is suppressed by the short time-gate. In both plots for the feed array the previous discussed overcompensation can be recognized towards the end of the X-band.

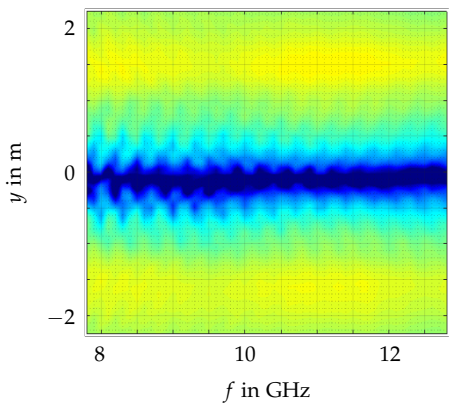

Fig. 4.9: Cross-polar level of the QZ field generated by the reference feed over frequency. The time-gate has a length of 250 cm.

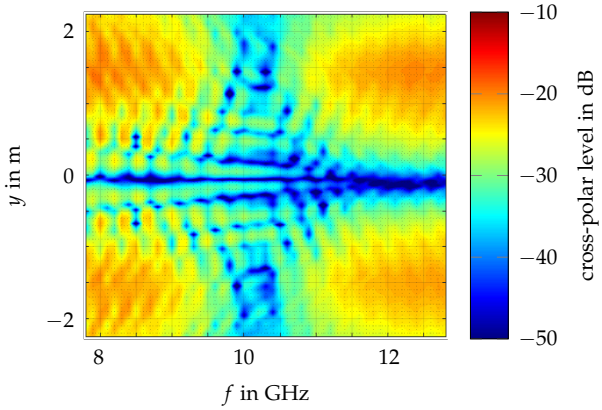

Fig. 4.10: The measured cross-polar level of the QZ field generated by the feed array in the X-band. The time-gate has a length of 250 cm.

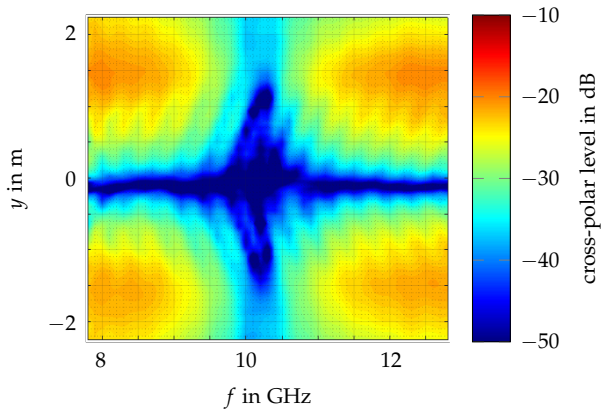

Fig. 4.11: Cross-polar level of the QZ field generated by the feed array. The time-gate has a length of 150 cm.

5 Conclusion and Outlook

The CTR of the Microwaves and Radar Institute of the DLR was analyzed regarding the cross-polarization purity of the QZ. The analysis regarded the currently used reference feed in the X-band. First investigations were made in the simulation software HFSS. The obtained results were verified by scanning the field distribution with a field probe. Especially towards the upper and lower end of the main-reflector an increased cross-polar level is found. Based on these findings a new feed array, consisting of three horn elements was developed and manufactured. It makes use of the conjugate matched field concept and reduces the cross-polarization level significantly. The complex weighting factors of each element were determined by a numerical optimization of the simulated near fields. An algorithm based on the interior points method was used, which had also considered the limitations of the prototype-based feeding network.

Especially the bandwidth of the compensation is restricted by the network, so the feed array was optimized to have the best cross-polarization performance around 10 GHz. The mean cross-polar level is decreased from -32.5 dB to -41.6 dB. An effective improvement of the cross-polar level is achieved in a band of 900 MHz. All discussed results are obtained in h-pol configuration, but of course, the principle can also applied to generate a vertically polarized field. A validation by field probe measurements for this configuration is a task for further investigation.

The reference feed uses a conical impedance wall, to suppress a direct illumination of the main-reflector. For the feed array it was not possible to use an impedance wall, because due to the increased size of the antenna it was not possible to mount it. In the obtained measurements the direct illumination was removed by a time-gating, but for a real use an impedance wall is needed for the feed array. This is a task for additional improvements in the future.

Table 5.1: Comparison of the mean cross-polar level ($\bar{b}$) between reference feed and feed array with the correct excitation of phase(w_{co})

	reference feed	feed array
8.2 GHz	-33.1 dB	-39.8 dB
9 GHz	-32.5 dB	-40.6 dB
10 GHz	-32.4 dB	-40.7 dB
11 GHz	-32.2 dB	-40.0 dB
12.4 GHz	-31.7 dB	-38.3 dB

Table 5.2: Comparison of the $b_{<\text{-}35\,\text{dB}}$ value between reference feed and feed array with the correct excitation of phase(w_{co})

	reference feed	feed array
8.2 GHz	31.7 %	76.5 %
9 GHz	28.6 %	79.0 %
10 GHz	28.2 %	80.9 %
11 GHz	27.7 %	78.3 %
12.4 GHz	29.2 %	67.6 %

An important step in the future is to replace the phase shifters in the feeding network by a filter. In Fig. 3.12 the optimized phase weighting factor for the co-horn is shown over the X-band. The conjugate matched field concept is very sensitive about changes in the phase, because it is based on destructive interference. In Tab. 5.1 and Tab. 5.2 the results for the feed array are simulated, if the correct excitation of phase(w_{co}) is ensured. For comparison the simulation results for the reference feed are shown as well. It can be seen that the correct excitation extends the cross-polarization compensation to the entire X-band. This can be achieved by a filter structure.

The function principle of the conjugate matched field concept and the three element feed array was proven successfully for the X-band, so that in future the cross-polarization in other frequency bands can be suppressed by modifying the array.

A Appendix

A.1 Reference Feed

The currently used reference feed for the CTR is a circular, corrugated horn. It was manufactured by March Microwave Systems B.V. and has the model number AF-0800/SL. For simulation purposes it is remodeled in Autodesk Inventor, the model is shown in Fig. A.1. In Fig. A.2 the simulated radiation pattern is shown. The co-polar pattern is nearly rotationally symmetric. The reference feed uses an impedance wall to suppress the direct illumination of the main-reflector, to avoid triple reflections. It is visualized in Fig. A.3.

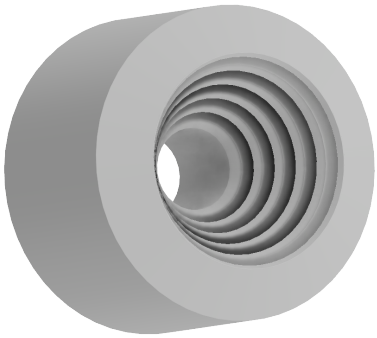

Fig. A.1: The remodeled reference feed (AF-0800/SL).

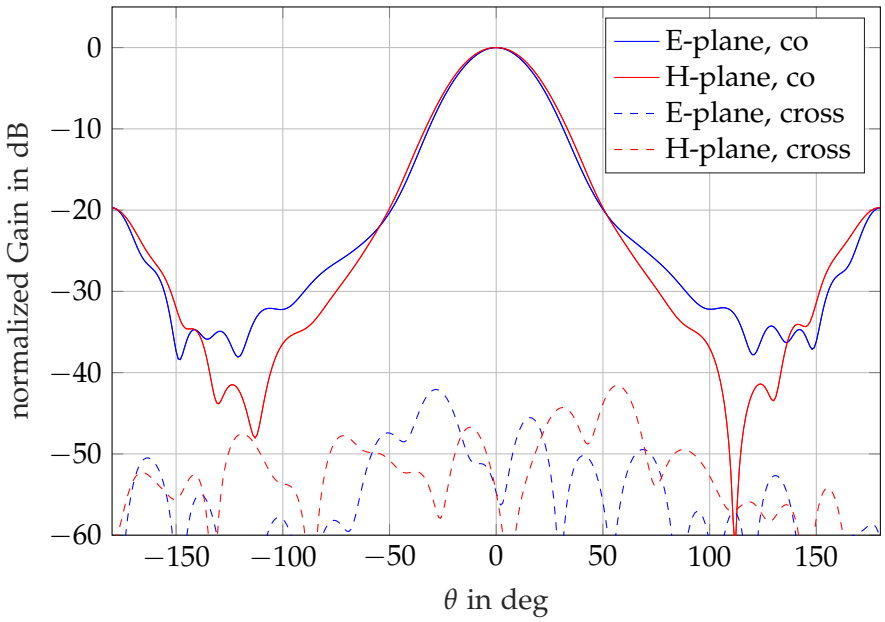

Fig. A.2: The radiation pattern of the reference horn at 10 GHz.

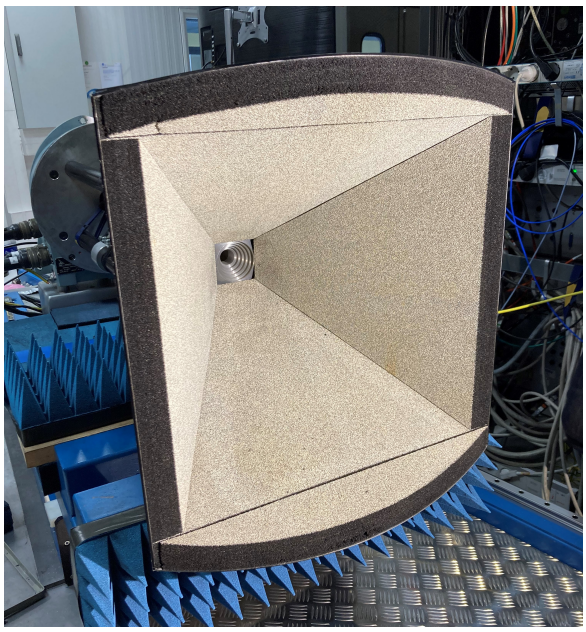

Fig. A.3: The impedance wall for the AF-0800/SL feed, to minimize the triple reflections.

A.2 Cross-Polarization in CTR of Reference Feed

In Fig. 3.1 and Fig. 3.2 the simulated cross-polar level is shown, when the CTR is excited by the reference feed. Both plots are obtained at a frequency of 10 GHz. In Fig. A.4 and Fig. A.5 the simulated cross-polar level is shown for the horizontal polarized reference feed, at 8.2 GHz respectively 12.4 GHz. In Fig. A.6 and Fig. A.7 the same is illustrated for the vertical polarized feed. In both cases an improvement in the cross-polar level for higher frequencies is visible.

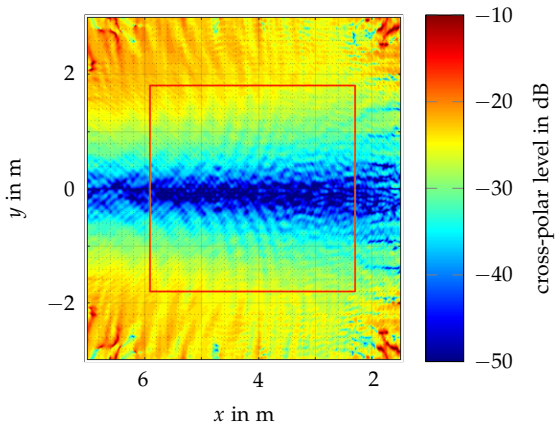

Fig. A.4: Horizontal polarized reference feed at 8.2 GHz.

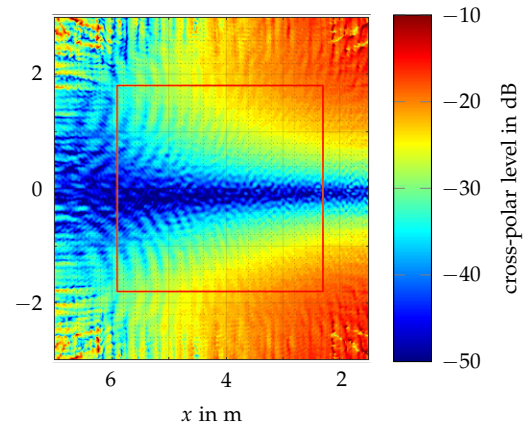

Fig. A.5: Horizontal polarized reference feed at 12.4 GHz.

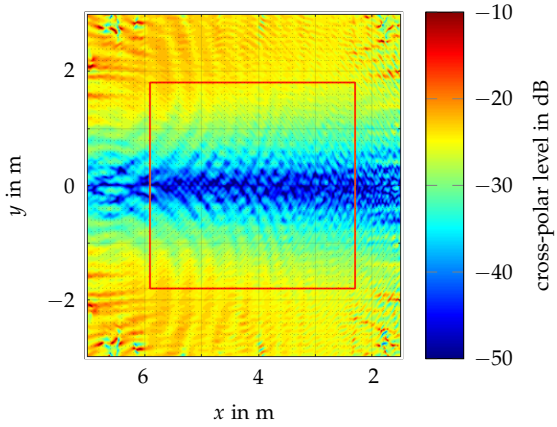

Fig. A.6: Vertical polarized reference feed at 8.2 GHz.

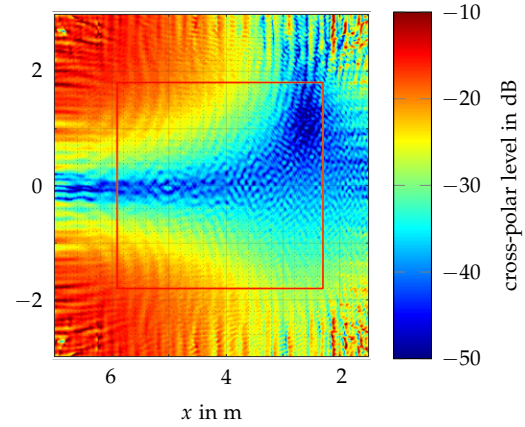

Fig. A.7: Vertical polarized reference feed at 12.4 GHz.

A.3 Cross-Polarization in CTR of Feed Array

The Fig 4.3 shows the simulated cross-polar level of the CTR equipped with the feed array at 10 GHz. For completeness the following two figures show the cross-polar level for 8.2 GHz and 12.4 GHz, in h-pol configuration. The weighting factors for the array elements are visualized in Fig. 3.11 and Fig. 3.12. In both figures the limited cross-polarization compensation is visible, since the optimized values for phase(w_{co}) can not be realized with the feeding network.

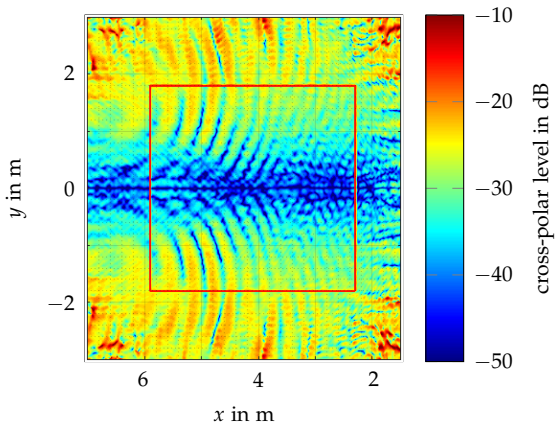

Fig. A.8: Horizontal polarized feed at 8.2 GHz.

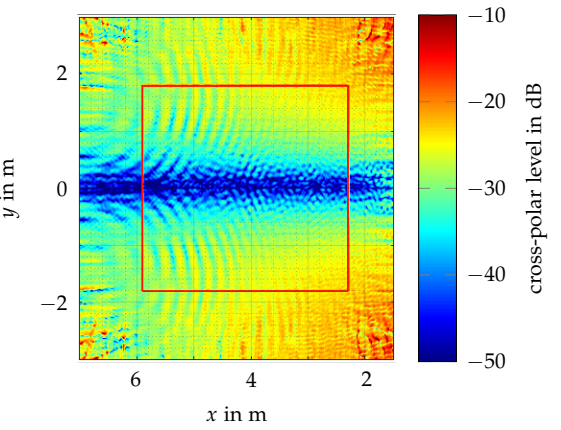

Fig. A.9: Horizontal polarized feed at 12.4 GHz.

A.4 Optimized Weighting Factors in the X-band

The following tables summarize the optimized weighting factors in the X-band. A single frequency optimization, see Section 3.2.4, is performed at 8.2 GHz, 9 GHz, 11 GHz and 12.4 GHz. Any limitations of the feeding network are not considered.

Table A.1: Optimized weighting factors at 8.2 GHz

		w_{co}	w_{cross1}	w_{cross2}
v-pol	$\lvert w\rvert$	1 W	1.11 mW	1.11 mW
	phase(w)	6.1°	0°	180.3°
h-pol	$\lvert w\rvert$	1 W	1.26 mW	1.26 mW
	phase(w)	186.1°	0°	179.2°

Table A.2: Optimized weighting factors at 9 GHz

		w_{co}	w_{cross1}	w_{cross2}
v-pol	$\lvert w\rvert$	1 W	1.03 mW	1.03 mW
	phase(w)	−36.5°	0°	180.4°
h-pol	$\lvert w\rvert$	1 W	1.26 mW	1.26 mW
	phase(w)	143.9°	0°	178.1°

Table A.3: Optimized weighting factors at 11 GHz

		w_{co}	w_{cross1}	w_{cross2}
v-pol	$\lvert w\rvert$	1 W	0.85 mW	0.85 mW
	phase(w)	−130.3°	0°	179.6°
h-pol	$\lvert w\rvert$	1 W	1.18 mW	1.18 mW
	phase(w)	45.1°	0°	181.5°

Table A.4: Optimized weighting factors at 12.4 GHz

		w_{co}	w_{cross1}	w_{cross2}
v-pol	$\lvert w\rvert$	1 W	0.78 mW	0.78 mW
	phase(w)	199.1°	0°	180.6°
h-pol	$\lvert w\rvert$	1 W	1.11 mW	1.11 mW
	phase(w)	−22.9°	0°	178.1°

A.5 Feed Array

In Fig. A.10 a technical drawing illustrates the dimensions of the new feed array. The axial distance between the cross-horns is variable and denoted by d.

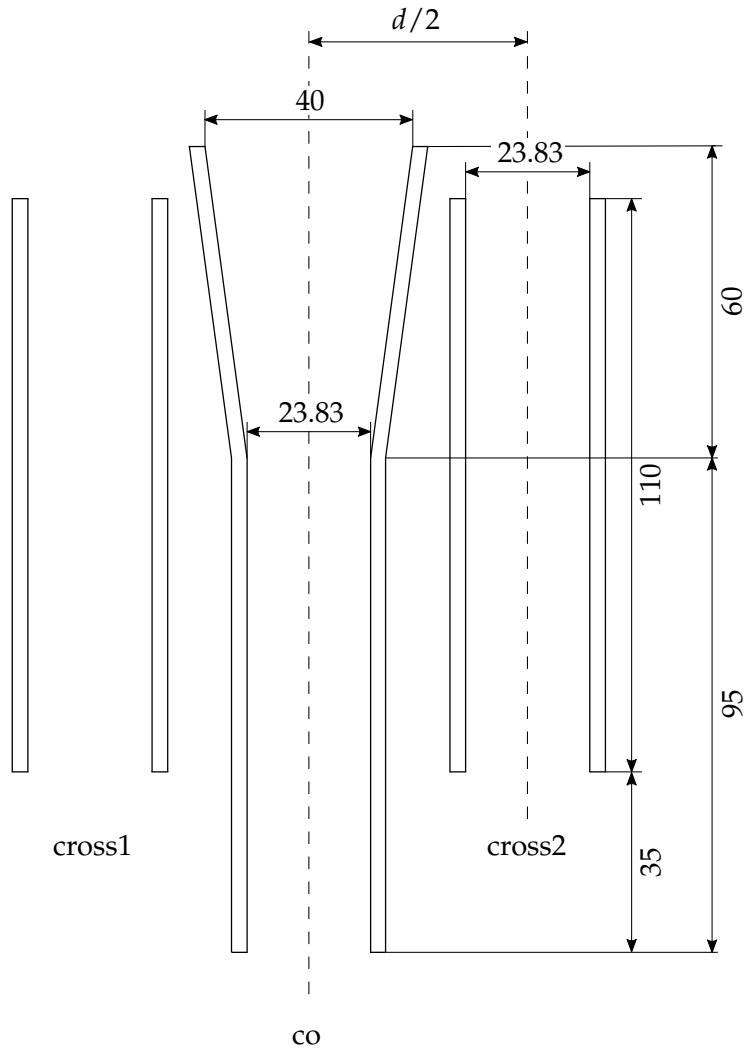

Fig. A.10: Dimensions of the feed array in millimeter.

A.6 Chamber Measurements

On May 6th, 2019 March Microwave Systems B.V. performed several measurements of the geometry of the CTR. The results are shown in Fig. A.11.

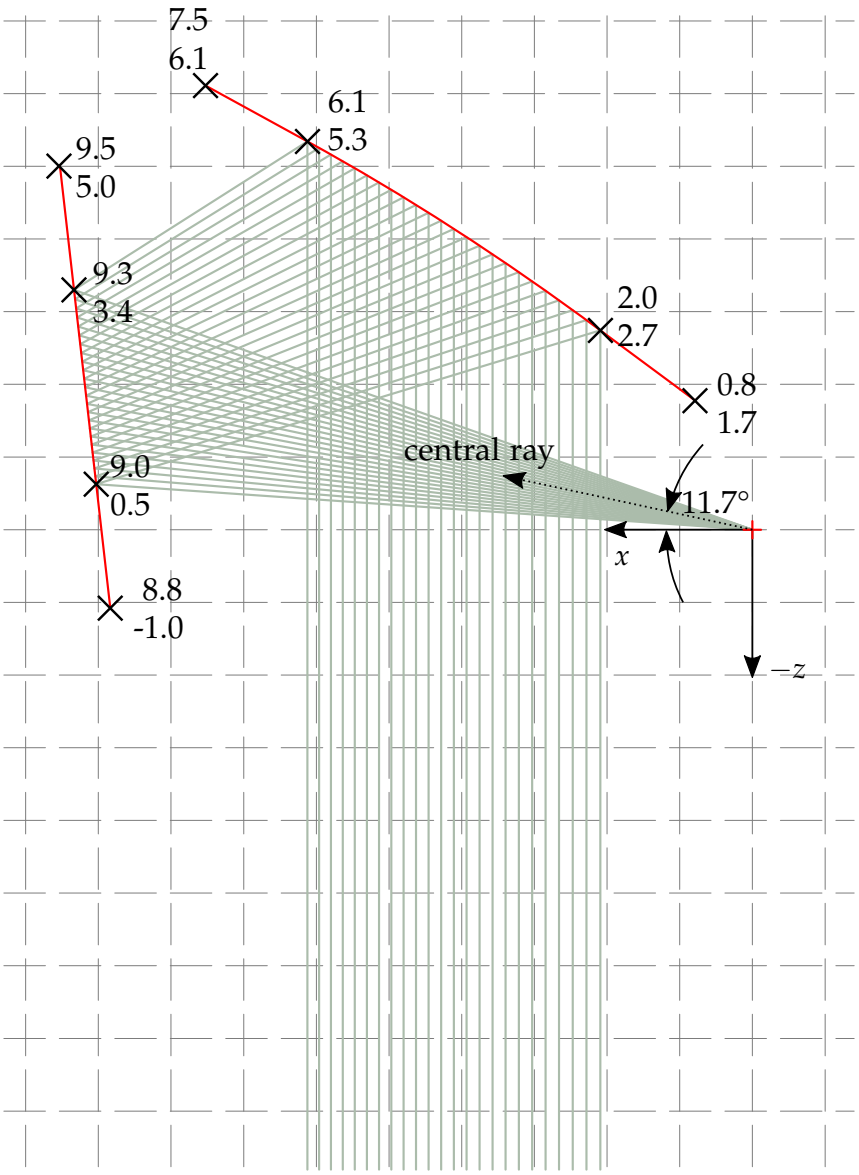

Fig. A.11: The chamber geometry with the measured values of all relevant points. All measurements are in meter.

Bibliography

[1] G. W. Stimson, H. Griffiths, C. Baker, and D. Adamy, *Stimson's Introduction to Airborne Radar*, 3rd ed. Edison, New Jersey, United States: SciTech Publishing, 2014.

[2] I. Hajnsek and P. Matteo, *Exploitation of fully polarimetric SAR data for application demonstrations (PolSAR-Ap)*, [Online], Available: `https://www.dlr.de/hr/desktopdefault.aspx/tabid-8352/14245_read-36019/`, (visited on 24/08/2022), 2021.

[3] I. Hajnsek and Y.-L. Desnos, *Polarimetric Synthetic Aperture Radar - Principles and Application*, 1st ed. Singapore, Singapore: Springer Nature, 2021.

[4] T.-S. Chu and R. Turrin, "Depolarization properties of offset reflector antennas," *IEEE Transactions on Antennas and Propagation*, vol. 21, no. 3, pp. 339–345, 1973.

[5] M. Sanad and L. Shafai, "Cross-polarization on the aperture of a compact range using dual parabolic cylindrical reflectors," in *Symposium on Antenna Technology and Applied Electromagnetics (ANTEM)*, Winnipeg, Canada, 1986, pp. 1–9.

[6] D. Fasold, "Measurement perfomance of basic compact range concepts," in *European Antenna Measurement Techniques Association Symposium (AMTA)*, Munich, Germany, 2006, pp. 1–11.

[7] H. Jiacai and H. Guoyu, "On the design of polarization grids for application in CATR," in *International Conference on Microwave and Millimeter Wave Technology (ICMMT)*, 2002, pp. 840–843.

[8] K. Bahadori and Y. Rahmat-Samii, "Tri-mode horn feeds revisited: Cross-pol reduction in compact offset reflector antennas," *IEEE Transactions on Antennas and Propagation*, vol. 57, no. 9, pp. 2771–2775, 2009.

[9] L. J. Foged, A. Giacomini, A. Riccardi, *et al.*, "Dual polarized wideband feed with cross-polarization reduction and compensation properties for compact antenna test range," in *Antenna Measurement Techniques Association Symposium (AMTA)*, Tucson, Arizona, United States, 2014, pp. 57–62.

[10] C. A. Balanis, *Antenna Theory - Analysis and Design*, 4th ed. Hoboken, New Jersey, United States: John Wiley and Sons, 2016.

[11] V. Monebhurrun, D. G. Michelson, G. Brown, *et al.*, "IEEE standard definitions of terms for radio wave propagation," *IEEE Std 211-2018 (Revision of IEEE Std 211-1997)*, p. 38, 2019.

[12] K. W. Kark, *Antennen und Strahlungsfelder - Elektromagnetische Wellen auf Leitungen, im Freiraum und ihre Abstrahlung*, 5th ed. Berlin, Germany: Springer, 2014.

[13] W. L. Stutzman and G. A. Thiele, *Antenna Theory and Design*, 3rd ed. Hoboken, New Jersey, United States: John Wiley and Sons, 2012.

[14] W. L. Stutzman, *Polarization in Electromagnetic Systems*, 2nd ed. Norwood, Massachusetts, United States: Artech House, 2018.

[15] A. Roederer, E. Farr, L. Foged, and M. Francis, "IEEE standard for definitions of terms for antennas," *IEEE Std 145-2013 (Revision of IEEE Std 145-1993)*, pp. 11, 30, 2014.

[16] C. Parini, S. Gregson, J. McCormick, and D. J. v. Rensburg, *Theory and Practice of Modern Antenna Range Measurements*, 1st ed. London, United Kingdom: Institution of Engineering and Technology, 2014.

[17] A. Ludwig, "The definition of cross polarization," *IEEE Transactions on Antennas and Propagation*, vol. 21, no. 1, pp. 116–119, 1973.

[18] G. F. Masters and S. Gregson, "Coordinate system plotting for antenna measurements," Torrance, California, United States: Nearfield Systems Inc., 2007.

[19] J. Hartmann, J. Habersack, and H.-J. Steiner, "Antenna measurement in compact ranges," in *Workshop on Space Borne Antanna Technologies and Measurement Techniques (ISRO)*, Ahmedabad, India, 2002, pp. 2.1–2.13.

[20] Y. Mizugutch, M. Akagawa, and H. Yokoi, "Offset dual reflector antenna," in *Antennas and Propagation Society International Symposium*, vol. 14, Amherst, Massachusetts, United States, 1976, pp. 2–5.

[21] P. van de Coevering, "Part 2 compact antenna test range (CATR) model 8074b," March Microwave Systems B.V., Tech. Rep.

[22] M. A. Qureshi, C. H. Schmidt, and T. F. Eibert, "Efficient near-field far-field transformation for nonredundant sampling representation on arbitrary surfaces in near-field antenna measurements," *IEEE Transactions on Antennas and Propagation*, vol. 61, no. 4, pp. 2025–2033, 2013.

[23] M. H. Francis, L. Foged, D. Bodnar, *et al.*, "IEEE recommended practice for near-field antenna measurements," *IEEE Std 1720-2012*, pp. 19–90, 2012.

[24] M. Ulbrich and S. Ulbrich, *Nichtlineare Optimierung*, 1st ed. Berlin, Germany: Springer, 2012.

[25] J. D. Pintér, *Global Optimization - Scientific and Engineering Case Studies*, 1st ed. Berlin, Germany: Springer, 2006.

[26] W. Hochstättler, *Lineare Optimierung*, 1st ed. Berlin, Germany: Springer, 2017.

[27] S. Nickel, S. Rebennack, O. Stein, and K.-H. Waldmann, *Operations research*, 3rd ed. Berlin, Germany: Springer, 2022.

[28] D. G. Luenberger and Y. Ye, *Linear and Nonlinear Programming*, 4th ed. Berlin, Germany: Springer, 2015.

[29] L. Rade and B. Westergren, *Springers mathematische Formeln - Taschenbuch für Ingenieure, Naturwissenschaftler, Informatiker, Wirtschaftswissenschaftler*, 3rd ed. Berlin, Germany: Springer, 2000.

[30] *Ansys HFSS SBR+*, [Online], Available: `https://www.ansys.com/content/dam/resource-center/application-brief/ansys-sbr-plus.pdf`, (visited on 31/08/2022), 2018.

[31] L. G. T. van de Coevering, B. Gabler, and B. Möhring, "Improving measurement results by applying hybrid compact range modelling methods," in *European Conference on Antennas and Propagation (EuCAP)*, 2021, pp. 1–5.

[32] K. Nakamura and M. Ando, "A full-wave analysis of offset reflector antennas with polarization grids," *IEEE Transactions on Antennas and Propagation*, vol. 36, no. 2, pp. 164–170, 1988.

[33] E. Lier and S. Skyttemyr, "A shaped single reflector offset antenna with low cross-polarization fed by a lens horn," *IEEE Transactions on Antennas and Propagation*, vol. 42, no. 4, pp. 478–483, 1994.

[34] H. Lebret and S. Boyd, "Antenna array pattern synthesis via convex optimization," *IEEE Transactions on Signal Processing*, vol. 45, no. 3, pp. 526–532, 1997.

[35] *Matlab Help Center Fmincon*, [Online], Available: `www.mathworks.com/help/optim/ug/fmincon.html`, (visited on 22/08/2022), 2022.

[36] *Constrained Nonlinear Optimization Algorithms - MATLAB & Simulink - MathWorks Deutschland*, [Online], Available: `https://de.mathworks.com/help/optim/ug/constrained-nonlinear-optimization-algorithms.html`, (visited on 22/08/2022), 2022.

List of Figures

List of Tables